AGU PUBLICATIONS

JGR

Journal of Geophysical Research: Solid Earth

RESEARCH ARTICLE
10.1002/2016JB013557

Brittle and semibrittle creep of Tavel limestone deformed at room temperature

A. Nicolas[1], J. Fortin[1], J. B. Regnet[1], B. A. Verberne[2], O. Plümper[2], A. Dimanov[3], C. J. Spiers[2], and Y. Guéguen [1]

[1]Laboratoire de Géologie, Ecole Normale Supérieure-PSL Research University-CNRS, UMR 8538, Paris, France, [2]Department of Earth Sciences, Utrecht University, Utrecht, Netherlands, [3]Laboratoire de Mécanique des Solides, UMR 7649, Ecole Polytechnique, Bat 65, Route de Saclay, Palaiseau, France

Key Points:
- Brittle-ductile transition during creep at room temperature
- Creep is related to dilatancy under low confining pressure and is related to compaction then dilatancy under high confining pressure
- Micromechanisms of deformation switch from crack propagation to intracristalline plasticity with increasing confining pressure

Correspondence to:
A. Nicolas,
nicolas@geologie.ens.fr

Citation:
Nicolas, A., J. Fortin, J. B. Regnet, B. A. Verberne, O. Plümper, A. Dimanov, C. J. Spiers, and Y. Guéguen (2017), Brittle and semibrittle creep of Tavel limestone deformed at room temperature, *J. Geophys. Res. Solid Earth*, *122*, 4436–4459, doi:10.1002/2016JB013557.

Received 15 SEP 2016
Accepted 2 JUN 2017
Accepted article online 6 JUN 2017
Published online 28 JUN 2017

Abstract Deformation and failure mode of carbonate rocks depend on the confining pressure. In this study, the mechanical behavior of a limestone with an initial porosity of 14.7% is investigated at constant stress. At confining pressures below 55 MPa, dilatancy associated with microfracturing occurs during constant stress steps, ultimately leading to failure, similar to creep in other brittle media. At confining pressures higher than 55 MPa, depending on applied differential stress, inelastic compaction occurs, accommodated by crystal plasticity and characterized by constant ultrasonic wave velocities, or dilatancy resulting from nucleation and propagation of cracks due to local stress concentrations associated with dislocation pileups, ultimately causing failure. Strain rates during secondary creep preceding dilative brittle failure are sensitive to stress, while rates during compactive creep exhibit an insensitivity to stress indicative of the operation of crystal plasticity, in agreement with elastic wave velocity evolution and microstructural observations.

1. Introduction

Rock failure occurs due to the coalescence of cracks caused by the accumulation of damage governed by (1) the increase of applied stress or (2) the progressive time-dependent growth of microcracks, even at constant stress [e.g., *Olsson*, 1974]. In the latter case, failure occurs by static fatigue because subcritical crack growth (see review by *Atkinson* [1984]) leads to a localization of damage (see review by *Brantut et al.* [2013]). Subcritical crack growth was observed in brittle media such as glasses [*Orowan*, 1944; *Charles*, 1958; *Wiederhorn and Bolz*, 1970; *Swanson*, 1984; *Mallet et al.*, 2014, 2015a], sandstones [*Holder et al.*, 2001; *Heap et al.*, 2009a], granites [*Kranz*, 1979; *Swanson*, 1984; *Lockner*, 1993; *Wang et al.*, 2015a], shales [*Swanson*, 1984], basalts [*Swanson*, 1984; *Heap et al.*, 2011], gabbros [*Meredith and Atkinson*, 1985], or limestones [*Rutter*, 1972; *Eslami et al.*, 2012; *Brantut et al.*, 2013, 2014], among other rock types [*Atkinson and Meredith*, 1987], and modeled micromechanically [e.g., *Amitrano and Helmstetter*, 2006; *Brantut et al.*, 2012; *Mallet et al.*, 2015a; *Wang et al.*, 2015b].

The mechanical behavior of limestones is highly sensitive to changes in confining pressure. In particular, they undergo a brittle-ductile transition at room temperature [*Heard*, 1960; *Byerlee*, 1968; *Renner and Rummel*, 1996; *Wong and Baud*, 2012]. As shown by previous studies, the brittle-ductile transition depends on several parameters such as grain size, porosity, and pore size [*Fredrich et al.*, 1990; *Vajdova et al.*, 2004, 2010; *Zhu et al.*, 2010; *Wong and Baud*, 2012]. When deformed at confining pressures below the brittle-ductile transition, samples undergo (1) elastic compaction until a point beyond which (2) dilatancy occurs, leading to (3) a stress drop denoting macroscopic failure. Brittle micromechanisms of deformation are propagation and coalescence of microcracks, inducing shear localization and a sudden strength loss [*Brace*, 1978; *Baud et al.*, 2000a; *Vajdova et al.*, 2004, 2010]. When triaxially deformed at confining pressures above the brittle-ductile transition, samples first exhibit elastic compaction followed by shear-enhanced compaction [e.g., *Baud et al.*, 2000a; *Vajdova et al.*, 2004]. The micromechanisms operative during shear-enhanced compaction are microcracking, cataclastic pore collapse, grain rotation, or grain-scale plastic flow (crystal plasticity and constant volume diffusive mass transfer) [*Paterson*, 1978; *Fredrich et al.*, 1989; *Evans et al.*, 1990; *Dresen and Evans*, 1993; *Renner and Rummel*, 1996; *Paterson and Wong*, 2005; *Zhu et al.*, 2010; *Dautriat et al.*, 2011]. Calcite can deform by processes such as mechanical twinning or *r*-, *f*-dislocation glide even at room temperature [*Turner et al.*, 1954; *Griggs et al.*, 1960; *De Bresser and Spiers*, 1993, 1997]. However, in porous limestones as in other types of rocks,

inelastic compaction is a transient phenomenon, and as differential stress increases, volumetric strain becomes dilatant beyond a critical state [*Baud et al.*, 2000a], showing that crack nucleation and/or propagation becomes dominant [e.g., *Baud et al.*, 2000a; *Nicolas et al.*, 2016]. For intermediate confining pressures and room temperature, *Fredrich et al.* [1989] showed that Carrara marble with a low porosity of $\leq$1% exhibits semibrittle behavior, involving macroscopically distributed deformation by both crystal plasticity (twinning and dislocation glide) and microcracking associated with dilatancy [see also *Evans et al.*, 1990; *Dresen and Evans*, 1993]. The complex interplay of plasticity and crack propagation was investigated by *Schubnel et al.* [2005] on low-porosity ($\phi = 0.5 - 4.5\%$) carbonate rocks, and *Rutter* [1972] showed that changes in the form of the stress-strain curves recorded for samples of Solnhofen limestone ($\phi = 5.8\%$) deformed at various confining pressures and strain rates could be explained by simultaneous operation of thermally activated intracrystalline deformation mechanisms and athermal frictional sliding processes. Microplasticity can interact with, annihilate, or enhance crack nucleation and growth [*Stroh*, 1954; *McMeeking*, 1977; *Kinloch and Williams*, 1980; *Dresen and Evans*, 1993; *Faleskog and Shih*, 1997; *Brantut*, 2015; *Cheng et al.*, 2016; *Covey-Crump et al.*, 2016]. *Brantut* [2015] also showed a possible, fast recovery of the microstructure due to a combination of backsliding on wing cracks and pressure solution.

The various micromechanisms involved in the deformation of carbonate rocks pose a challenge to predicting the mechanical behavior at constant stress. *Brantut et al.* [2014] showed that brittle creep was taking place in Purbeck limestone ($\phi = 13.8\%$, quartz content of 20%). Their experiments were conducted under water-saturated conditions, enabling mechanisms such as pressure solution and stress corrosion cracking, as discussed in their article. Water decreases the surface energy, promotes subcritical crack growth and stress corrosion in many brittle media [*Rebinder et al.*, 1948; *Clarke et al.*, 1986; *Atkinson and Meredith*, 1987; *Costin*, 1987; *Baud et al.*, 2000b; *Røyne et al.*, 2011; *Liteanu et al.*, 2013; *Mallet et al.*, 2015b]. Under water-saturated conditions, brittle strength of carbonate rocks is reduced [e.g., *Rutter*, 1974; *De Bresser et al.*, 2005; *Nicolas et al.*, 2016] but this effect seems to decrease with increasing temperature because of a change of micromechanisms of deformation [*De Bresser et al.*, 2005].

To the authors' knowledge, the mechanical behavior of limestones at constant stress and room temperature for confining pressures above the brittle-ductile transition has not yet been investigated in detail. *Rutter* [1972, 1974] examined the effect of strain rate on the mechanical behavior of low-porosity carbonate rocks. Yet semibrittle behavior is observed in some natural settings [e.g., *Ross and Lewis*, 1989] and as it involves different micromechanisms of deformation [e.g., *Fredrich et al.*, 1989] with different kinetics, changes of boundary conditions from controlled strain rate to controlled stress could lead to a different partitioning of the micromechanisms of deformation with implications on the mechanical stability. This study focuses on the mechanical behavior of white Tavel limestone (initial porosity of 14.7%) at constant differential stress. We address the following questions: (1) What are the micromechanisms involved in the deformation at constant stress (creep) in porous limestones? (2) Which micromechanism controls the deformation rate depending on the stress state (confining pressure and differential stress)?

We report results of triaxial stress-stepping creep experiments performed at various effective confining pressures in the range of 20–85 MPa to investigate the influence of confining pressure and differential stress on creep strain rate. In addition, evolution of *P* and *S* wave velocities was monitored during the experiments to infer processes associated with microcracks and quantifying damage evolution [e.g., *Schubnel et al.*, 2006; *Benson et al.*, 2006; *Fortin et al.*, 2007].

2. Experimental Methods

2.1. Rock Material and Sample Preparation

Experiments were performed on white Tavel limestone, the same material as used by *Vincké et al.* [1998]; *Vajdova et al.* [2004, 2010]; *Nicolas et al.* [2016]. Its composition is almost 100% calcite [*Vajdova et al.*, 2004]. This rock is mainly composed of micrite particles (mean diameter ~5 μm) cemented together, leading to micritic aggregates (Figures 1a and 1b). In this micritic layout, some micropores (diameter between 2 μm and 10 μm) can be observed in sparitic parts, where cementation or recrystallization of preexisting bioclasts remained incomplete (Figures 1a and 1c). Observations on ion beam-polished thin sections reveal the presence of a low initial crack porosity, located between micritic aggregates and/or micrite particles (Figure 1d).

Cylindrical samples of 40 mm in diameter and 86 mm in length were cored from the same block as the one used in *Nicolas et al.* [2016]. The ends of the cylinders were ground flat ensuring parallelism. Samples were

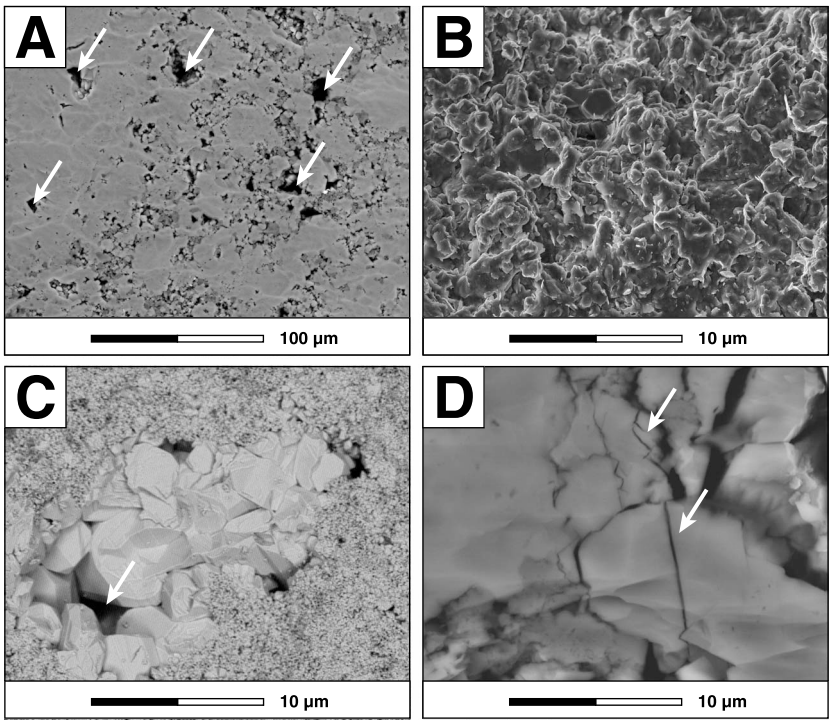

Figure 1. Micrographs of Tavel limestone in scanning electron microscope modified after *Nicolas et al.* [2016]. (a) General observations of the microstructure. Micropores (white arrows) can be observed between or within micritic aggregates. (b) Micritic aggregate composed of coarse anhedral micrite particles (≥4 µm) with fused to nonrecognizable contacts. (c) Incomplete sparitic cementation in a preexisting bioclast is at the origin of the largest pores (white arrow). (d) Micritic aggregate observed on an ion beam-polished thin section exhibiting initial crack porosity (regular or wing cracks, white arrows).

dried at ~40°C for several days and were then left to ambient humidity for 1 to 2 days while gluing the acoustic sensors (see section 2.3) prior to deformation.

Porosity was obtained from two measurements: (1) using the density of dried samples assuming that the rock is composed of 100% calcite and (2) using a triple weight procedure, i.e., by comparing the weight of a dry sample with that after water saturation, and the weight measured while totally immersing the saturated sample in water. These two methods give similar results, implying that all the porosity is connected. The average porosity is 14.7%, with maximum porosity variations of about 0.5%.

2.2. Experimental Apparatus

Triaxial deformation experiments were performed using the previously described conventional triaxial cell installed in the Laboratoire de Géologie at the École Normale Supérieure in Paris [*Ougier-Simonin et al.*, 2011; *Brantut et al.*, 2011]. Axial strain ε_{ax} of the samples was measured using four axial strain gauges (*Tokyo Sokki TML* type FCB 2-11) glued directly onto the sample and three displacement transducers (DCDT) mounted outside the pressure vessel and corrected for the stiffness of the loading frame using the strain gauge measurements. For both, strain gauges and DCDTs, we consider the mean value of the measurements to eliminate possible local effects. We do not use the axial strain gauges except for the correction of the DCDT data; because of the large axial strains ($\varepsilon_{ax} \geq 2\%$) attainable in carbonate rocks, the strain gauges tend to break, whereas DCDTs have no strain limitation. Radial strains ε_r are measured with four radial strain gauges. Uncertainty in strain measured with gauges is estimated to be of the order of 10^{-5}; DCDT signals have a lower accuracy of about 10^{-4}. The volumetric strain is calculated as $\varepsilon_v = \varepsilon_{ax} + 2\varepsilon_r$.

In this paper, compressive stresses and compactive strains are taken positive. Principal stresses will be denoted σ_1 and σ_3, σ_1 corresponding to the highest principal stress (axial stress) and σ_3 to the confining pressure, P_c. Differential stress $\sigma_1 - \sigma_3$ and mean stress $(\sigma_1 + 2\sigma_3)/3$ will be denoted Q and P, respectively.

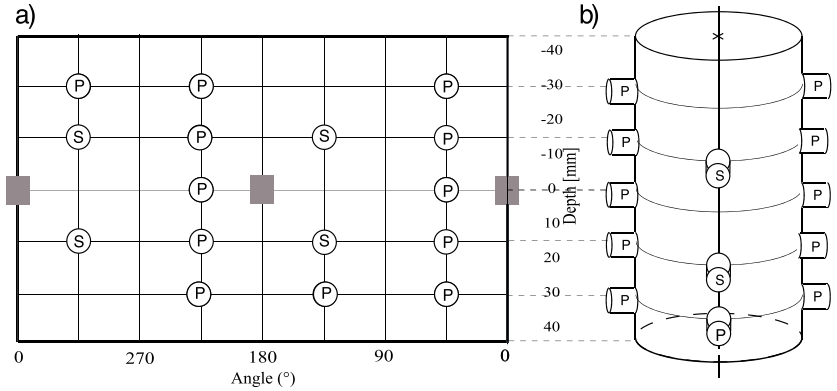

Figure 2. (a) Sensor map used for the experiments. *S* wave velocities were measured on directions perpendicular to the sample axis. *P* wave velocities were measured on directions forming an angle of 34°, 42°, 53°, 70°, and 90° with the sample axis. (b) A schematic view of a prepared sample.

2.3. Ultrasonic Wave Velocities

Sixteen piezoelectric transducers (PZTs) were directly glued onto the sample surface, four sensitive to *S* waves and the others to *P* waves. Both types of PZT sensors have a resonant frequency around 1 MHz. All transducers can be used either as receivers (in passive mode) or as sources (in active mode). A thorough description of the acoustic system can be found in *Ougier-Simonin et al.* [2011] and *Brantut et al.* [2011]. No significant acoustic emission activity was recorded, so PZTs were used in the active mode to measure the evolution of *P* and *S* wave velocities during deformation. Depending on the experiment duration, ultrasonic velocity surveys are recorded every 1, 5, or 30 min. The arrival time is corrected for the samples' axial and radial deformation. The PZT sensor arrangement (Figure 2) yields *P* wave velocities along five different angles with respect to the symmetry axis, i.e., at 90° (ray perpendicular to the main axis); 70°, 53°, 42° and 34°. In addition, velocities of horizontally and vertically polarized shear waves (S_h and S_v) are measured at an angle of 90° (radial). Arrival times are measured to an accuracy of 0.1 μs, leading to a precision of the absolute velocities of ≃5% and a relative precision of ≃0.2%.

2.4. Mechanical Behavior During Constant Strain Rate Deformation and Experimental Procedure for Creep

Results of constant strain rate experiments ($\dot{\varepsilon}_{ax} \sim 10^{-5}$ s^{-1}) conducted on dry Tavel limestone at confining pressure between 0 and 85 MPa (Figure 3) were presented in a previous study [*Nicolas et al.*, 2016]. Here we give a brief summary of their results, which are needed to understand the present experimental procedure. For $P_c \leq 55$ MPa, the observed features are typical of the brittle regime: (i) samples undergo elastic compaction until a stress level denoted *C′* [*Wong et al.*, 1997], beyond which dilatancy takes place (Figure 3b); (ii) the differential stress reaches a peak, beyond which strain softening occurs; and (iii) observation of the samples after deformation demonstrates that the deformation was localized on a shear fracture. For $P_c \geq 70$ MPa, samples exhibit (1) an elastic compaction and (2) an inelastic shear-enhanced compaction associated with strain hardening beyond a critical stress denoted *C** [*Wong et al.*, 1997] (Figure 3b). Yet the inelastic compaction is transient and volumetric strain reverses to dilatancy beyond a critical stress denoted *C*′* [*Baud et al.*, 2000a] (Figure 3 b). These features involve macroscopically distributed deformation by both crystal plasticity and microcracking, lead to final axial strains in the range of 3–5% at failure, and induce a pressure-dependent strength, which are typical of the semibrittle regime (a subclass of the ductile regime) as defined by *Evans et al.* [1990]. Semibrittle deformation as defined by *Evans et al.* [1990] envisions the competition between brittle mechanisms and crystal plasticity in dense aggregates. In porous aggregates, the brittle-ductile transition can be defined as the transition from localized failure with stress drop after little deformation to significant permanent deformation accommodated by macroscopically nonlocalized cataclasis. In that sense, the deformation of samples that undergo nonlocalized inelastic compaction but head to failure with stress drop after significant straining can be classified as semibrittle. In this manuscript, samples that undergo dilatancy beyond the elastic domain and exhibit a stress drop after little inelastic deformation will be considered as brittle and samples that undergo nonlocalized inelastic compaction will be considered as semibrittle. The brittle-ductile transition occurs at 55 MPa $\leq P_c \leq$ 70 MPa for this Tavel limestone deformed at a constant strain rate of $\sim 10^{-5}$ s^{-1}.

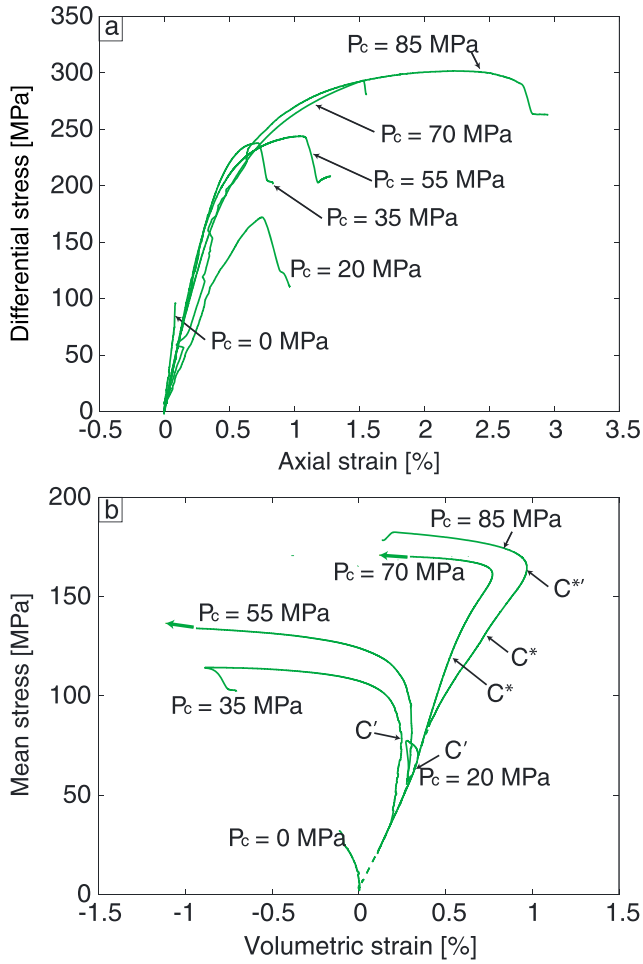

Figure 3. Compilation of mechanical data for constant strain rate experiments [modified after *Nicolas et al.*, 2016]. (a) Differential stress versus axial strain curves for experiments performed in dry conditions. (b) Mean stress versus volumetric strain curves for experiments performed in dry conditions.

In this study our goal is to investigate the mechanical behavior of Tavel limestone during brittle and semibrittle creep. Stress-stepping creep experiments are conducted at confining pressures covering the brittle-ductile transition inferred from constant strain rate experiments, i.e., from 20 to 85 MPa. During the experiments, the pore system is left open and the pore space of the samples is connected to ambient air. Samples are deformed using a constant imposed differential stress (creep experiments). Samples are first loaded hydrostatically up to the desired confining pressure, followed by triaxial loading using a constant imposed axial strain rate ($\sim 10^{-5}$ s^{-1}) until the target differential stress is reached (Table 1). A key point before starting stress-stepping creep experiments is to determine the level of differential stress to be applied during the first stress step. In the brittle regime, below the onset of dilatancy (*C′*), the rock is assumed to be elastic; thus, the differential stress should be higher than *C′* to observe time-dependent processes. In the semibrittle regime, the first stress step is performed between the threshold for inelastic compaction *C** and the postyield dilatancy *C*′*. The stress state is maintained for extended periods of time (from 24 h to 48 h), allowing the samples to deform at constant stress. This procedure is repeated for *n* steps in differential stress (Figure 4) following a stress-stepping procedure [*Heap et al.*, 2009a, 2011; *Mallet et al.*, 2015a; *Liu and Shao*, 2016], until failure of the samples.

2.5. Sample Recovery and Microstructural Analysis

For each value of confining pressure used in our experiments (20, 35, 55, 70, and 85 MPa, see Table 1), we recovered samples for microstructural investigation. The deformed samples were impregnated with blue-dyed epoxy resin and, after curing for several days, sectioned along a plane parallel to the principal loading axis. Sections covered the entire deformed sample, i.e., measuring ~8 cm by ~4 cm, and were polished to a thickness of ~30 μm.

Table 1. Summary of the Mechanical Data for Stress-Stepping Creep Experiments Performed on White Tavel Limestone[a]

N°	P_{eff} (MPa)	Different Stress (MPa)	Min$\{\dot{\epsilon}_{ax}\}$ (s^{-1})	Duration (Hours)	Final Axial Strain (%)	Notes
1	20	144.4	$2.17\ 10^{-9}$	22.1	0.615	
		146.6	$2.56\ 10^{-9}$	19.3	0.02637	
		149.53	$2.66\ 10^{-9}$	22.6	0.03889	
		152.93	$2.21\ 10^{-9}$	33.1	0.05429	
		155.43	$2.67\ 10^{-9}$	16.4	0.0265	
		161.33	$2.14\ 10^{-8}$	4.8	0.0603	failure
2	35	237.8	$4.47\ 10^{-7}$	1.05	0.02	failure
3	35	195.4	$6.11\ 10^{-9}$	42.9	1.554	
		206.4	$2.51\ 10^{-7}$	1.5	0.2	failure
4	55	9.3	$5.19\ 10^{-10}$	19.9	0.02757	
		224.3	$2.04\ 10^{-9}$	28.2	0.5902	
		275	$1.04\ 10^{-6}$	1.9	0.8725	failure
5	55	150	$9.11\ 10^{-10}$	22.3	0.5982	
		165	$8.06\ 10^{-10}$	22.4	0.07689	
		170	$1.48\ 10^{-9}$	25.9	0.03068	
		175	$1.79\ 10^{-9}$	23.1	0.042	
		181	$2.77\ 10^{-9}$	25.8	0.03854	
		191	$2.45\ 10^{-9}$	24.8	0.085	
		201	$4.17\ 10^{-9}$	22.8	0.1048	
		206	$4.17\ 10^{-9}$	22.3	0.06267	
		211	$4.72\ 10^{-9}$	25	0.06707	
		218.6	$7.22\ 10^{-9}$	25.4	0.1202	
		228.2	$8.06\ 10^{-9}$	22.3	0.2121	
		238.5	$6.67\ 10^{-9}$	49.9	0.485	
		243.7	$7.78\ 10^{-9}$	46.2	0.2168	
		279	$1.25\ 10^{-8}$	73.2	0.513	failure
6	70	210.6	$3.06\ 10^{-9}$	20.8	0.8386	
		260	$5.56\ 10^{-9}$	24.7	0.5762	
		306.2	$8.27\ 10^{-7}$	0.4	2.523	failure
7	70	263.6	$1.31\ 10^{-8}$	70.8	4.56	
		267.3	$1.47\ 10^{-8}$	23.9	0.1681	
		271	$1.47\ 10^{-8}$	30.2	0.2385	
		275	$2.08\ 10^{-8}$	23	0.2272	
		280.6	$2.42\ 10^{-8}$	47.4	1.063	
		288.6	$3.74\ 10^{-7}$	0.1	0.03901	failure
8	85	204.5	$4.72\ 10^{-9}$	24.5	1.118	
		304.6	$3.33\ 10^{-8}$	24.3	5.275	
		354.3	-	24.4	1.768	EPS
9	85	215.3	$8.61\ 10^{-9}$	26.8	1.586	
		265.3	$3.53\ 10^{-8}$	23.4	2.778	
		290.4	$6.22\ 10^{-8}$	20.1	3.88	
		294	$4.81\ 10^{-8}$	27.1	0.5675	
		300.7	$6.39\ 10^{-8}$	21.4	0.6025	
		322	$1.53\ 10^{-7}$	48.3	0.7793	EPS

[a]EPS denotes end of piston stroke.

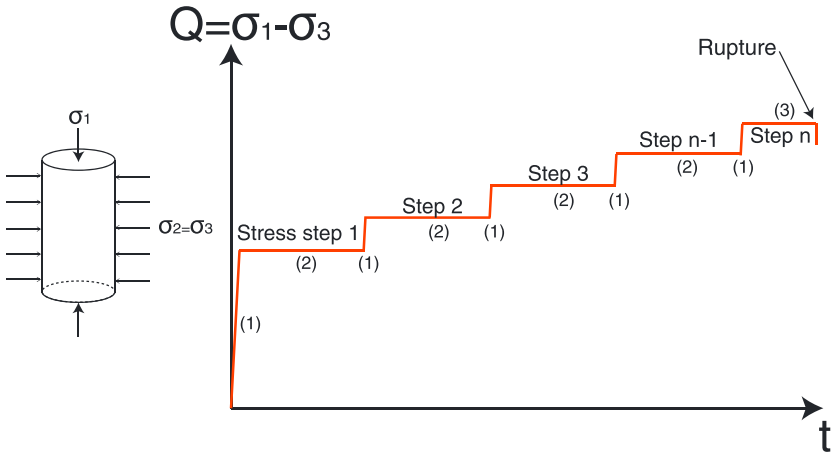

Figure 4. Experimental protocol for stress-stepping creep tests. During phases noted (1), the differential stress is increased with a constant strain rate procedure, during (2), the differential stress is maintained constant for several hours. The phase (3) corresponds to the last step, during which macroscopic failure occurs.

Transmitted light analyses of thin sections were performed using a Leica DMRXP optical polarizing light microscope (OPM). Selected samples were analyzed using a Zeiss Sigma scanning electron microscope (SEM-FEG), using a FEI Helios Nanolab G3 focused ion beam (FIB)-SEM, and using a FEI Talos F200x transmission electron microscope (TEM). Scanning electron microscopy imaging was typically done in backscatter electron (BSE) mode, employing an acceleration voltage of 15 kV and beam current of ~1 nA. We used FIB-SEM to prepare electron transparent foils from calcite single crystals with a thickness of ~50–100 nm [e.g., *Wirth*, 2009] measuring ~20 μm by ~10 μm for TEM investigations.

3. Results

3.1. Mechanical Behavior Under Constant Stress

All experiments exhibit an elastic behavior during the first part of loading; then, the mechanical behavior depends upon the confining pressure (Figure 5).

3.1.1. Brittle Creep

First, we focus on experiments conducted at $P_c \leq 35$ MPa, where features observed in conventional triaxial experiments are typical of the brittle regime. In the experiment performed at $P_c = 20$ MPa, the first stress step was conducted at $Q = 144$ MPa (Figure 6a), above the critical stress C' ($Q_{C'} = 108$ MPa). The sample deformed by primary creep and then secondary creep (Figure 6a). After about 24 h, the differential stress was stepped up sequentially (Table 1) until the sample eventually failed (Figure 6a). All creep phases were associated with dilatancy (Figure 5c) and a decrease of ultrasonic velocities (Figure 7c). The decrease in *P* wave velocities is higher for the higher angles with respect to σ_1 (Figure 7c). Tertiary creep starts 40 min before failure, after a total axial strain of approximately 0.6%; the acceleration of axial strain rate is associated with a decrease of *P* wave velocity for all pathways. Volumetric strain switches from dilating constant volumetric strain rate to compaction prior to rupture. In this phase of creep close to failure, it is likely that the sample undergoes a localization of strain on a failure plane. The volumetric strain shows a local stress decrease near the developing failure plane, thus leading to a recompaction of this part of the dilating sample. At failure, the decrease in *P* wave velocity ranges from −5% at an angle of 90° to −1.7% at an angle of 34°.

3.1.2. Semibrittle Creep

Conventional triaxial experiments conducted on Tavel limestone at $P_c \geq 55$ MPa are typical of the semibrittle regime as defined in section 2.4. The first step of the experiment conducted at $P_c = 85$ MPa was performed at $Q = 215$ MPa (Figure 6c), between the critical stresses C^* ($Q_{C^*} = 144$ MPa) and $C^{*\prime}$ ($Q_{C^{*\prime}} = 267$ MPa). The sample deformed transiently between primary and secondary creep (Figure 6c). After about 27 h, the stress was stepped up to a differential stress *Q* of 265 MPa (Table 1), slightly lower than the postyield dilatancy ($C^{*\prime}$) inferred from constant strain rate experiments. This stepping procedure was then repeated sequentially beyond $C^{*\prime}$ until the piston reached its maximum displacement, which corresponds to an axial strain of 9.5% for this experiment. The first step of this experiment is associated with compaction and the following ones with dilation (Figure 5b).

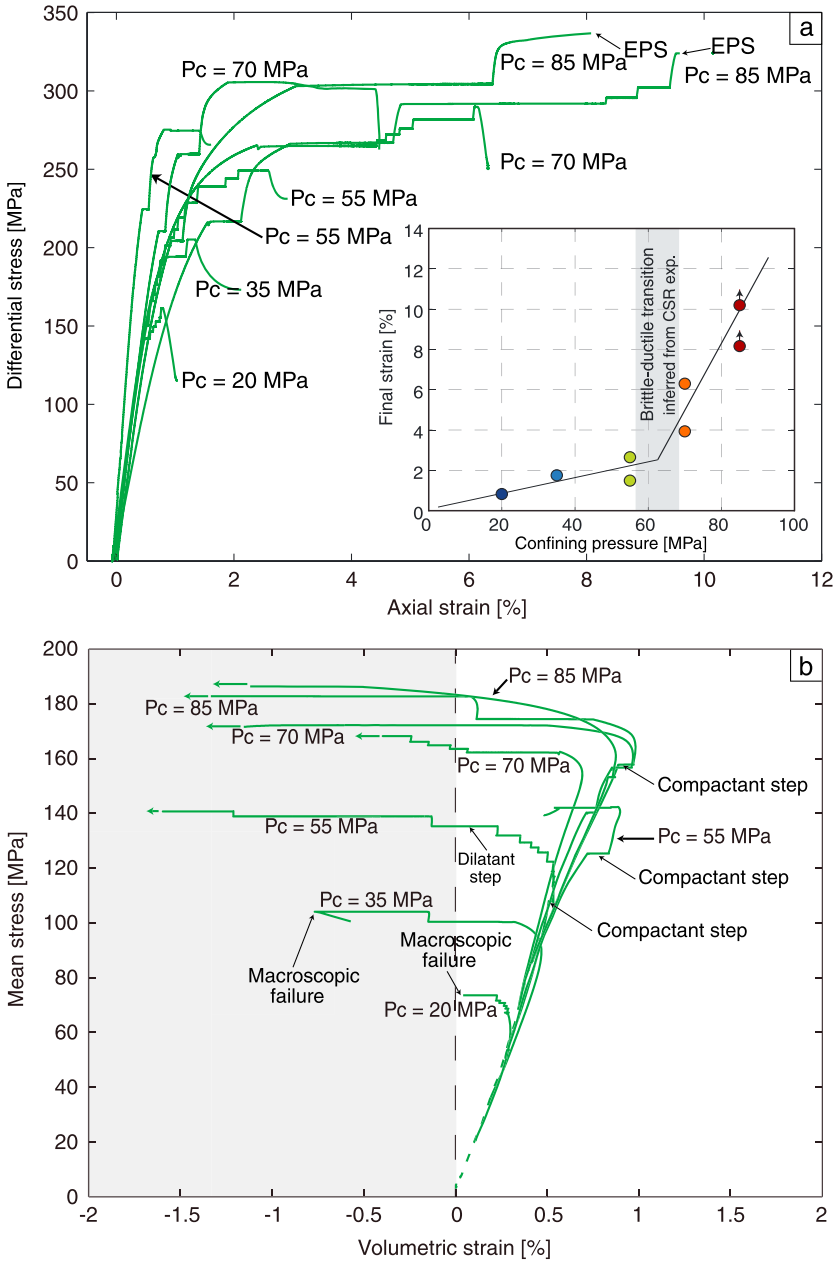

Figure 5. Compilation of mechanical data obtained during stress-stepping creep experiments. (a) Differential stress versus axial strain. The inset shows the final strains reached at the macroscopic failure as a function of the confining pressure. Brown arrows indicate that the piston reached its maximum displacement before failure. The shadowed area corresponds to the brittle-ductile transition inferred from the constant strain rate experiments conducted by *Nicolas et al.* [2016]. (b) The mean stress versus volumetric strain curves for stress-stepping creep experiments are shown. Horizontal arrows indicate that radial strain gauges broke, preventing us from recording the volumetric strain any further. EPS means that the moving piston reached its maximum displacement.

We first focus on the compactive first step of this experiment (Figure 8). During secondary creep, the axial strain rate was 8.6×10^{-9} s^{-1} (Figure 8 a and Table 1). The secondary creep was associated with (i) compaction and (ii) constant ultrasonic wave velocities at all angles (Figure 8b). Compaction reached 0.08% at the end of the stress step.

During the second stress step of this experiment (Figure 9), ultrasonic wave velocities decreased during primary creep, by 1% to 2.5% depending on the angle with respect to σ_1. The maximum decrease was observed for the pathway perpendicular to σ_1 (Figure 9b). During secondary creep, the axial strain rate was 3.5×10^{-8} s^{-1}

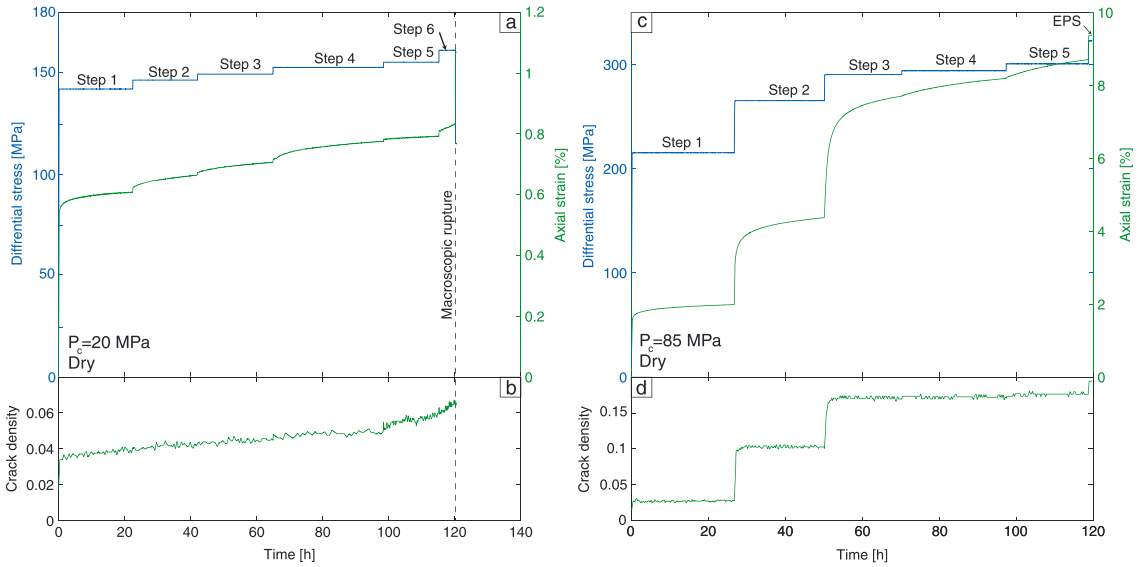

Figure 6. Evolution of the differential stress and axial strain for creep stepping experiments at (a) $P_c = 20$ MPa and (c) $P_c = 85$ MPa, and (b and d) corresponding evolutions in inverted crack density.

(Figure 9a and Table 1). For this second step, secondary creep was associated with (i) dilatancy (Figure 9a) and (ii) constant ultrasonic wave velocities at all angles (Figure 9b). Dilation reached a value of −0.6% at the end of this second stress step. Failure did not occur during this experiment before the piston reached its maximum displacement. The fifth stress step is the last "full" step of this experiment. During this step, the differential stress Q was 300 MPa. Volumetric strain could not be recorded because the radial strain gauges had already reached their maximum strain limit. During secondary creep, the axial strain rate was 6.4×10^{-8} s^{-1} (Figure 10a and Table 1). The primary and secondary creep stages were associated with a decrease of ultrasonic wave velocities of 1%, independent of the angle of their pathway with respect to σ_1 (Figure 10b).

3.2. Crack Densities

To interpret the evolution of the ultrasonic velocities, we consider a porous rock made of a mixture of solid grains, spherical pores, and penny-shaped cracks of radius c and aperture w. Inverted crack densities offer a quantitative description of the damage due to cracks [*Nasseri et al.*, 2007; *Mallet et al.*, 2013, 2014; *Regnet et al.*, 2015a]. We use *Budiansky and O'Connell*'s [1976] definition of crack density ρ_c:

$$\rho_c = \frac{1}{V}\sum_{i=1}^{N} c_i^3, \tag{1}$$

where c_i is the radius of the ith crack and N is the total number of cracks embedded in the representative elementary volume V. Note that from equation (1), the dominant factor for the crack density is not the number of cracks per unit volume but the crack length c. *Mallet et al.* [2013, 2014] showed that crack densities inverted from ultrasonic velocities of a cracked glass were in very good agreement with optically measured ones. Here the concept of crack density is meant to take into account all kinds of nonspherical, flat, inclusions. For example, a porous space between two grains is considered to be a crack [*Guéguen and Kachanov*, 2011; *Ghabezloo*, 2015].

Our results show that ultrasonic wave velocities recorded under triaxial stress depend on the pathway (see, for example, Figure 7), indicating that cracks are not randomly oriented. The maximum decrease is observed for the pathway perpendicular to σ_1 (90°), which suggests that the propagating and/or nucleating cracks are mainly axial [*Mavko et al.*, 1995; *Ayling et al.*, 1995; *Fortin et al.*, 2011], in agreement with direct observations by *Olsson* [1974] on deformed limestone samples. As previously done by *Nicolas et al.* [2016] for the same material, we invert ultrasonic wave velocities to axial crack density [*Sayers and Kachanov*, 1995; *Mallet et al.*, 2013] assuming (1) a transverse isotropic geometry of axial cracks, reflecting that in our experiments $\sigma_2 = \sigma_3$; (2) an isotropic matrix, in agreement with the isotropic ultrasonic wave velocities measured under hydrostatic conditions [*Nicolas et al.*, 2016]; (3) noninteracting cracks, an assumption which is valid for crack densities

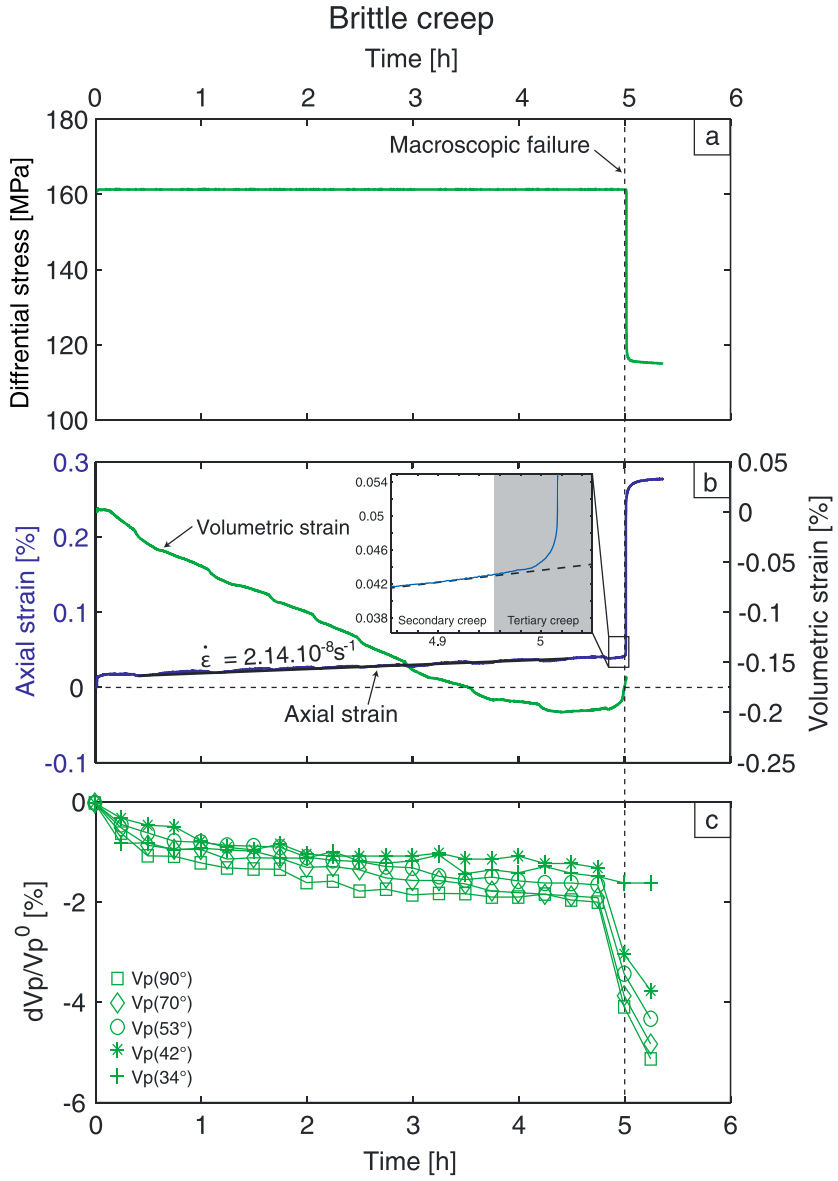

Figure 7. (a) Evolution of the differential stress during the last creep step of the experiment conducted at a confining pressure of 20 MPa. (b) Evolution of the axial and volumetric strains during this stress step. (c) Evolution of $\delta V_p/V_p^0$ (where V_p^0 is the *P* wave velocity at the end of the preceding constant strain rate loading) at different angles with respect to σ_1.

up to at least 0.15 and probably even 0.2–0.25 [*Grechka and Kachanov*, 2006]; and (4) a random crack center distribution. The effective mechanical properties of the calcite aggregate composed of the solid matrix and embedded pores (Young's modulus E_0 = 32.8 GPa and Poisson's ratio ν_0 = 0.29) were estimated from velocities measured at P_c = 85 MPa, a pressure far above the crack closing pressure in Tavel limestone [*Nicolas et al.*, 2016].

In the brittle regime, crack density increases for differential stresses above *C'*. Taking the experiment performed at P_c = 20 MPa as an example, crack density increased from 0.02 before triaxial loading to 0.065 at failure by tertiary creep (Figures 6b and 11a). During steps 1 to 5, crack density increased almost linearly with time (Figures 6b). However, during the last stress step, the rate of increase of the crack density accelerated.

In the semibrittle regime, the crack density evolution is different from what was observed in the brittle regime. Taking the experiment conducted at P_c = 85 MPa as an example, its initial crack density was 0.015 before

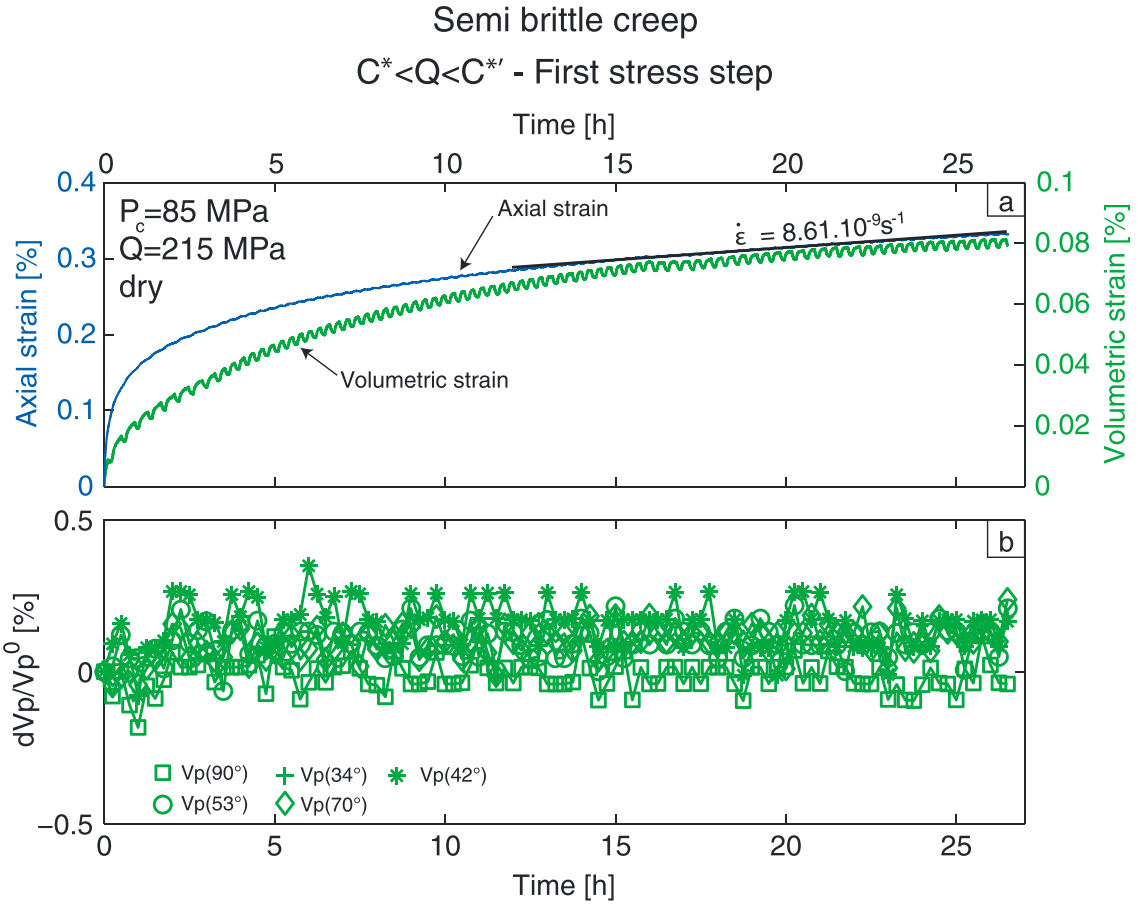

Figure 8. (a) Evolution of the axial and volumetric strains during the first creep step of the experiment done at P_c = 85 MPa. (b) Evolution of the $\delta V_p/V_p^0$ at different angles with respect to σ_1 during this creep step.

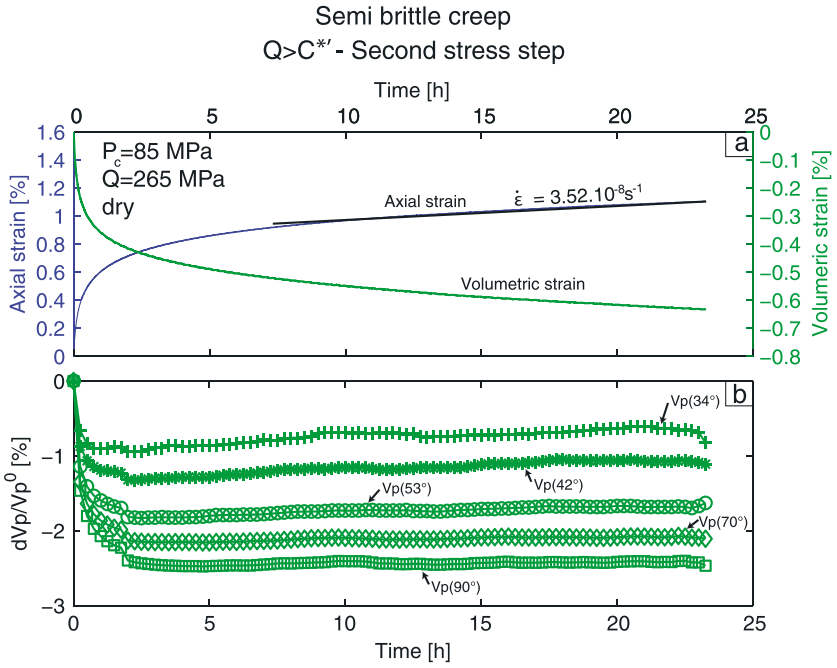

Figure 9. (a) Evolution of the axial and volumetric strains during the second creep step for the experiment done at P_c = 85 MPa. (b) Evolution of the $\delta V_p/V_p^0$ with respect to σ_1 during this creep step.

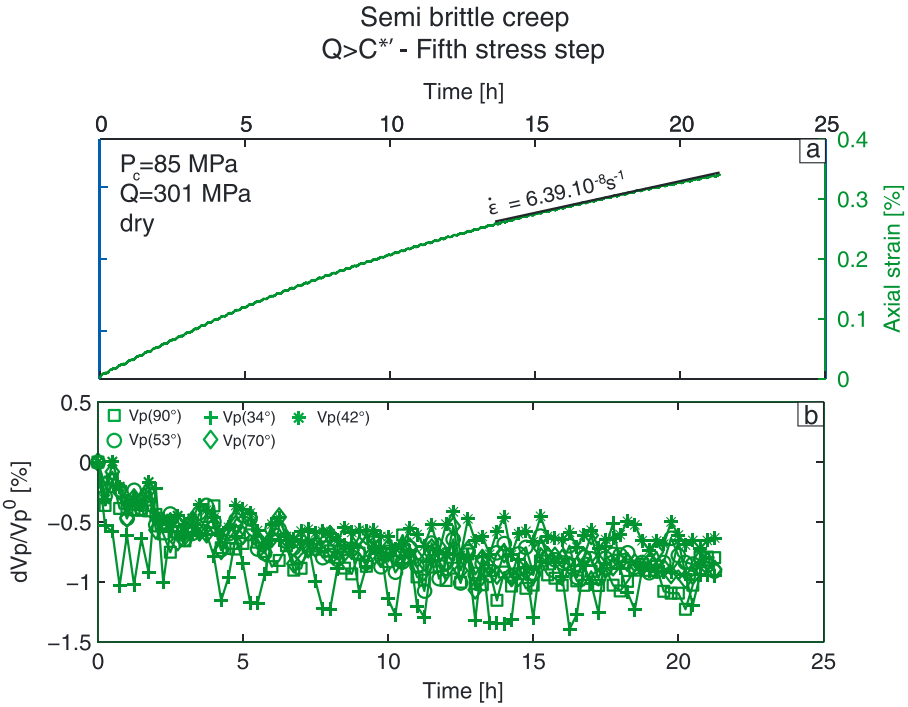

Figure 10. (a) Evolution of the axial strain during the fifth creep step of the experiment done at $P_c = 85$ MPa. (b) Evolution of the $\delta V_p/V_p^0$ at different angles with respect to σ_1 during this creep step.

triaxial loading (Figures 6d and 11b). Crack density increased up to 0.03 at the beginning of the first step and remained constant during this step. A similar behavior was observed for the next steps: the crack density remained constant at 0.1 during the second step, but at 0.017 during steps 3, 4, and 5. It reached 0.19 when the piston achieved its maximum displacement in step 6.

3.3. Strain Rates During Stress-Stepping Creep Experiments

At constant differential stress conditions, axial strain rate shows a deceleration (primary creep) before reaching a minimum strain rate (secondary creep) followed by, in some cases, an acceleration (tertiary creep) leading to macroscopic failure (e.g., Figure 7 and *Scholz* [1968] and *Lockner* [1993]). The minimum (secondary) strain rate is usually considered to reflect the strain rate sensitivity to stress.

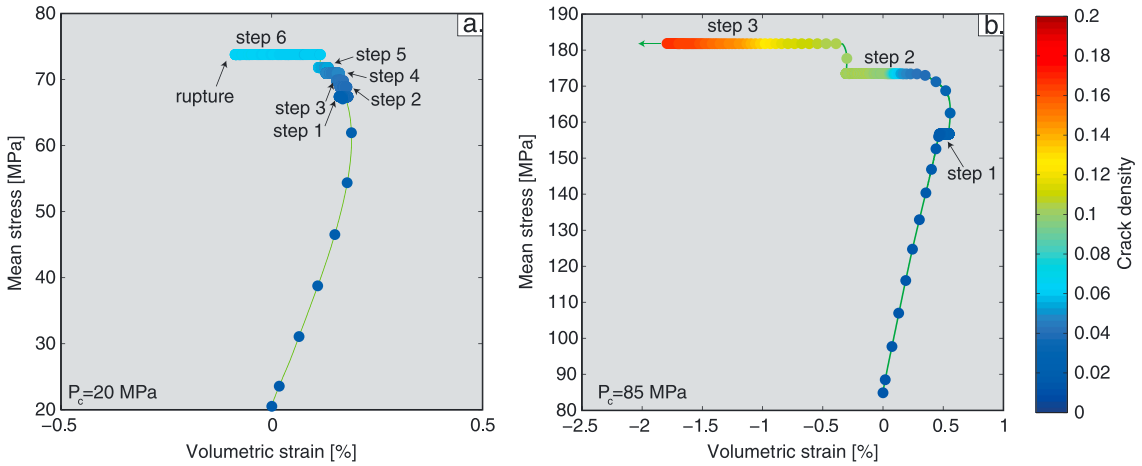

Figure 11. Volumetric strain is plotted as a function of mean stress for experiments performed at (a) $P_c = 20$ MPa and (b) $P_c = 85$ MPa. Crack density evolution is superimposed for each experiment. The color caption is given on the right.

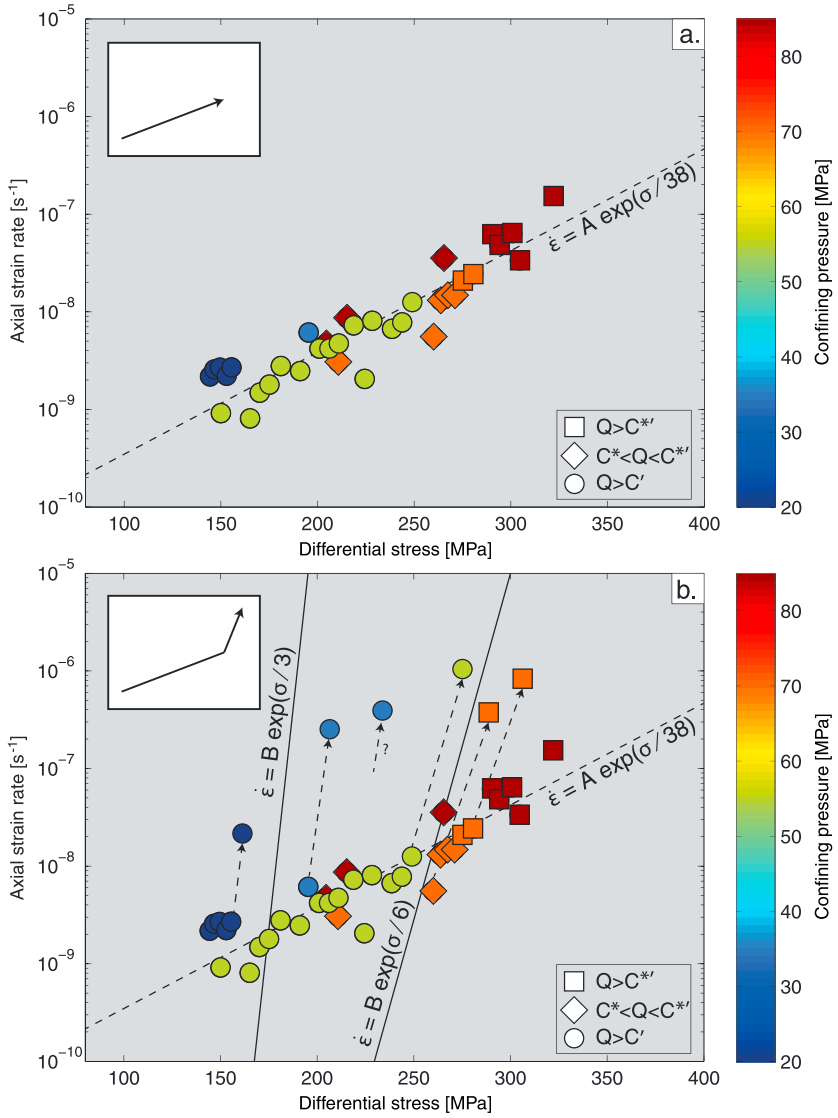

Figure 12. (a) Strain rates during secondary creep are plotted versus applied differential stress for stress-stepping creep experiments. In this figure, the minimum strain rate obtained during the last step of each experiment is not plotted. Symbols represent the stress state compared to stress states at the onset of dilatancy *C′*, onset of inelastic compaction *C** and postyield dilatancy *C*′* inferred from constant strain rate experiments. Note that constant strain rate experiment done at $P_c = 55$ MPa had a brittle behavior, but as the corresponding constant stress experiments are semibrittle as defined in section 2.4, the symbols were modified to semibrittle ones. The colors represent the confining pressure. The color caption is given on the right. The inset shows the schematic variation of the minimum strain rate variation as a function of the differential stress. (b) Same as Figure 12a for all stress steps, including the secondary creep measured during the last step of each experiment.

The minimum axial strain rates (from now on referred to as "minimum strain rates") of steps that did not lead to failure by tertiary creep (Figure 12a) depend on differential stress as

$$\dot{\varepsilon} \propto \exp\left(\frac{Q}{\sigma^*}\right), \tag{2}$$

where σ^* is an activation stress found to be $\sigma^* = 38$ MPa (Figure 12a). However, at $P_c = 20$ MPa, the minimum strain rate exhibits little variation with differential stress, which makes it hard to conclude for this confining pressure. Furthermore, only one point is available for $P_c = 35$; thus, the trend expressed by equation (2) is mainly reliable for $P_c \geq 50$ MPa, i.e., in the semibrittle regime.

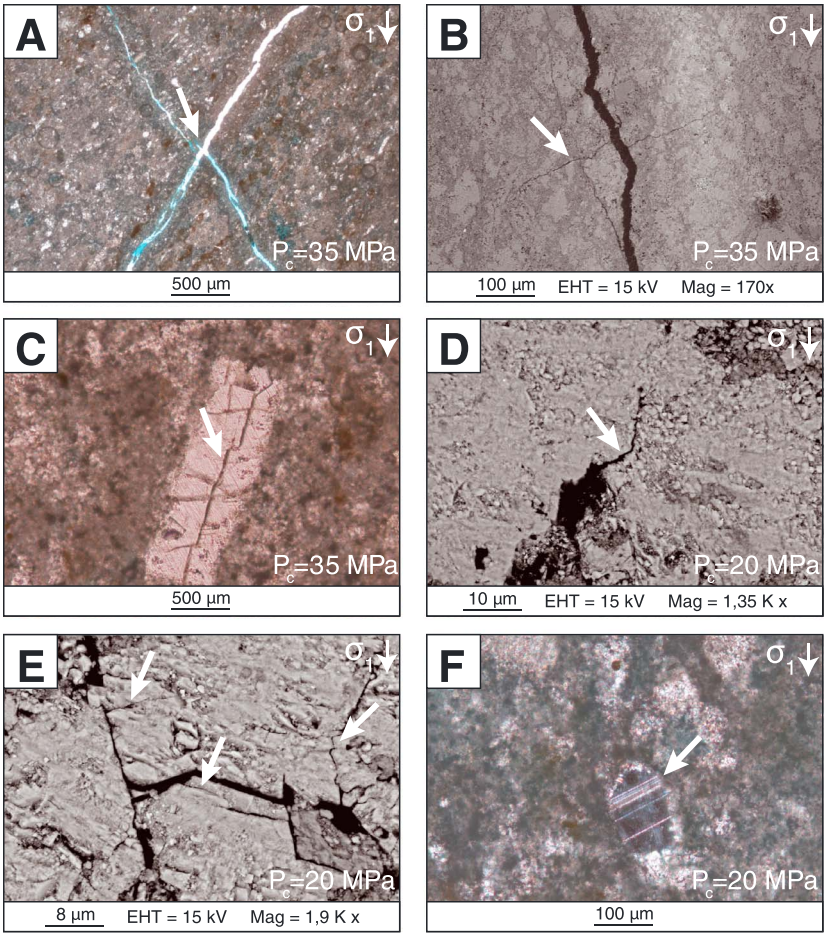

Figure 13. Micrographs of samples deformed at low confining pressure (20 MPa–35 MPa). (a) Shear fracture associated with the development of several fracture networks, observed under optical light. (b) A secondary network of fractures develops parallel and perpendicular to the main fracture. (c) In addition to the main fractures, microcracks appear to develop in larger calcite crystals. (d) Pore-emanated cracks develop around the biggest pores. (e) Cracks also propagate from grain contacts. (f) A very low twining activity is observed within the calcite crystals.

The minimum strain rates observed before failure, i.e., during the last stress steps of the experiments, do not follow the previous trend of the secondary creep rates (Figure 12b). A different activation stress applies to the two last stress steps for each experiment (Figure 12b). In the brittle regime ($P_c \leq 50$ MPa), the activation stress is found to be $\sigma^* = 3$ MPa. For experiments performed at $P_c \geq 50$ MPa (semibrittle regime), the second activation stress is found to be $\sigma^* = 6$ MPa, slightly higher than what was observed in the brittle regime. The occurrence of different activation stresses probably means different micromechanisms, which will be discussed in more detail in section 4.1.

3.4. Microstructures

Investigations with OPM and SEM revealed that samples that underwent stress-stepping creep deformation at low confining pressure (20 MPa–35 MPa) resulting in dilatancy (Figure 5b) show single, and sometimes conjugated, shear fractures, associated with the development of fracture networks perpendicular to the main fractures (Figures 13a and 13b). In addition to the larger centimeter-scale shear fractures, microcracks including wing cracks developed in the largest calcite crystals (Figure 13c) and are sometimes seen to emanate from pore walls (Figure 13d) as also observed by *Vajdova et al.* [2010] or micrite grain contacts (Figure 13e). However, a large proportion of the micritic grains do not show cracks. The number of twinned grains is low (Figure 13f). On the basis of visual inspection in an optical light microscope, the number of twinned grains in our deformed samples does not appear to be significantly different from the undeformed ones. Samples that underwent stress-stepping creep deformation at high confining pressure (70 MPa–85 MPa) and exhibited

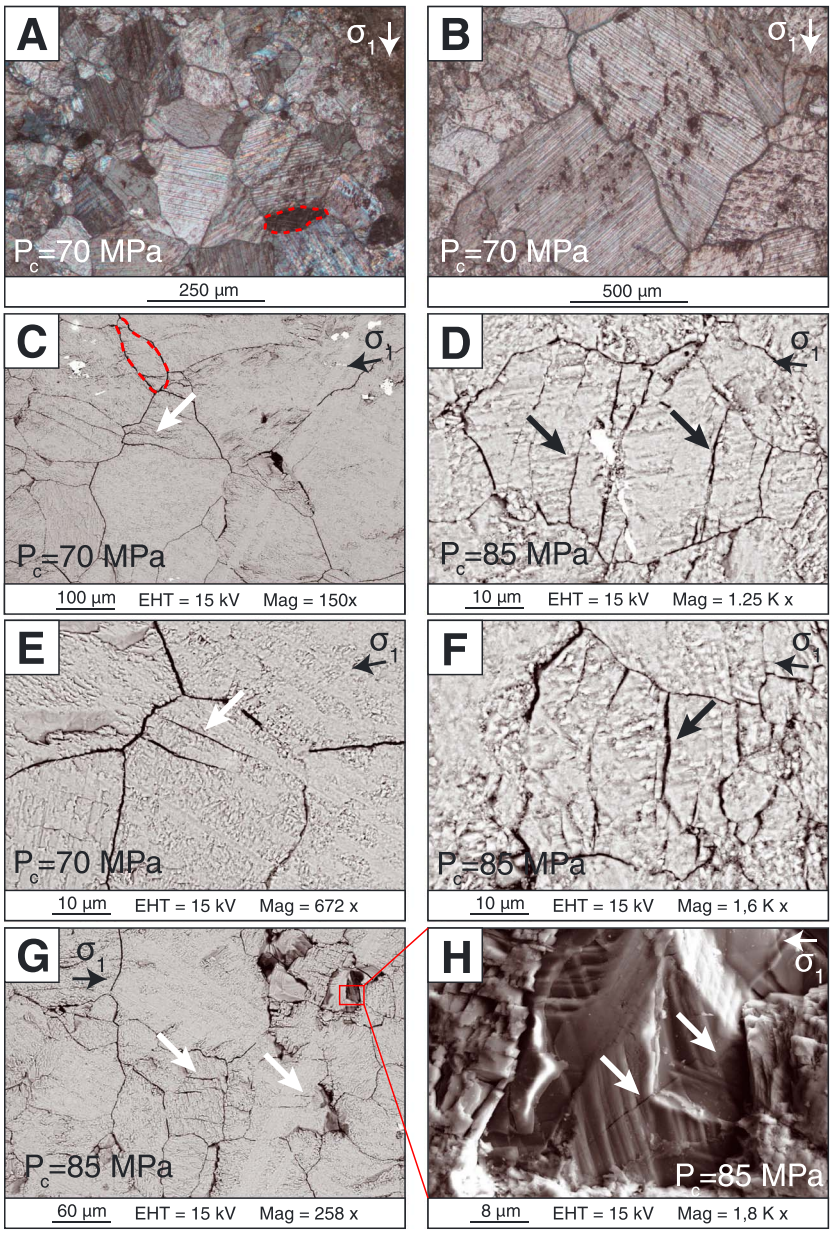

Figure 14. Micrographs of samples deformed at high confining pressure (70 MPa–85 MPa). (a and b) The twinning activity is very intense. (c–g) At some point corresponding to an inelastic compaction of about 0.5%, crystals cannot undergo more plastic strain and develop intragranular cracks. Cracks develop from grain boundaries (Figures 14c, 14e, and 14g) rather parallel to the major principal stress. (h) Cracks are cross cutting the twins.

shear-enhanced compaction followed by dilatancy show damage zones (Figure 14). Twinning is very intense (Figures 14a and 14b) and probably accounts for significant deformation until a point where crystals cannot undergo more plastic strain and develop cracks within the grains. At some locations, microcracks are seen to emanate from crystal centers (Figures 14d–14h). Cracks predominately developed subparallel to the maximum principal stress axis, cross cutting twinned grain domains. Significantly, cracks frequently stop at grain boundaries, implying that they do not propagate to adjacent grains (Figures 14c–14g).

Bright field TEM imaging shows a high dislocation density in a sample deformed in the semibrittle regime (Figure 15). The dislocation density is highest in the part of the crystal adjacent to the grain boundary (Figure 15e), suggesting that dislocations have piled up here (Figures 15d and 15e) or emanated from grain

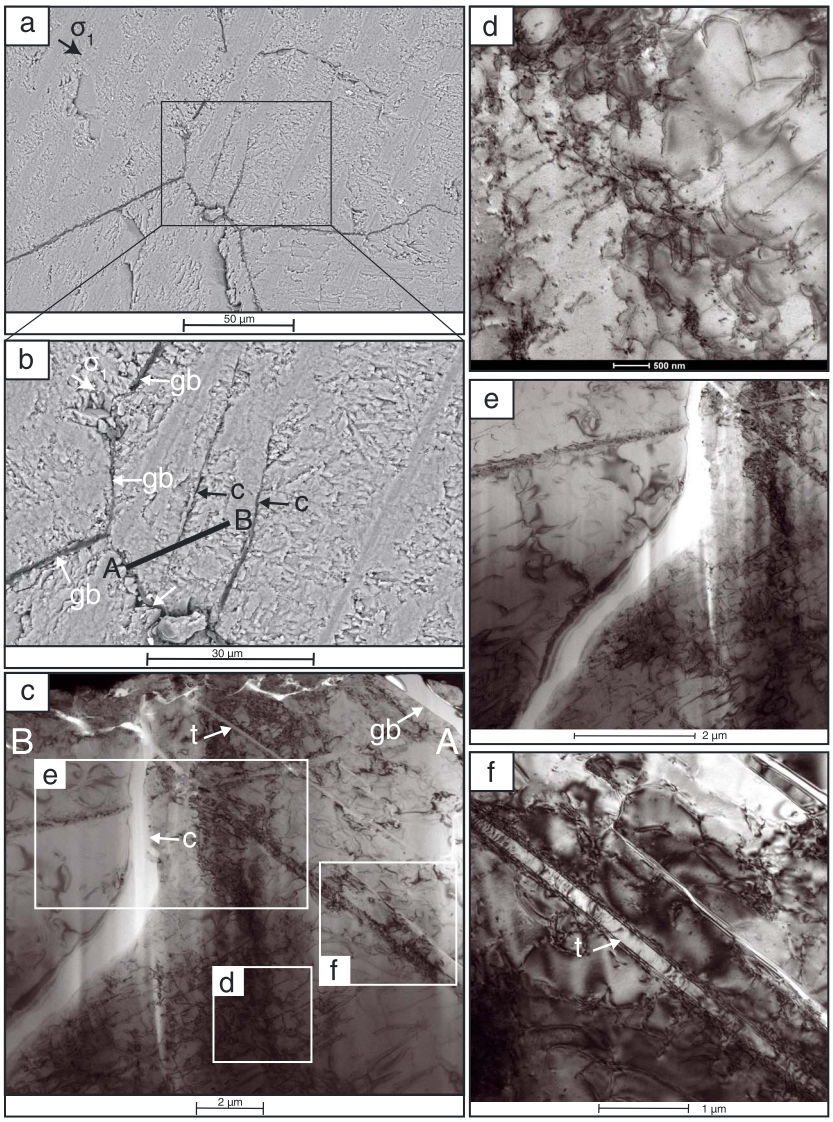

Figure 15. (a) Calcite crystals presenting a high twin density and intragranular cracks are identified in a sample deformed in the semibrittle regime (at P_c = 70 MPa). (b) A foil noted A-B was retrieved from a grain boundary (marked gb) to the middle of a single crystal, cross cutting a crack (marked c). Micrographs of a FIB-SEM foil retrieved from the single crystal. (c) Bright field transmission electron micrograph showing the foil recovered from the crystal showed in Figure 15b. The crack boundary is marked gb and the intragranular crack is marked c. Twins can be identified (marked t). The dislocation density is high in the area adjacent to the open grain boundary (marked gb). On the other side of the intragranular crack, the dislocation density is lower. (d) The area with high dislocation density is likely caused by dislocation pileup. (e) The difference of dislocation density between the two sides of the intragranular crack is high. On the right, next to the grain boundary, the dislocation density is much higher than on the left, in the middle of the grain. (f) The presence of twins is associated with a high dislocation density.

boundaries [e.g., *Hirth and Balluffi*, 1973]. On the other side of the intragranular crack (in the same calcite single crystal), the dislocation density is lower (Figure 15e), which might indicate that dislocations were absorbed at the crack surface. Twins are associated with a high dislocation density (Figure 15f).

4. Discussion

4.1. Mechanisms of Deformation

4.1.1. Brittle Creep

As in other materials, cracks in calcite can propagate subcritically in mode I [*Henry et al.*, 1977; *Dunning et al.*, 1994; *Røyne et al.*, 2008; *Rostom et al.*, 2013], which leads to possible time dependence of brittle failure

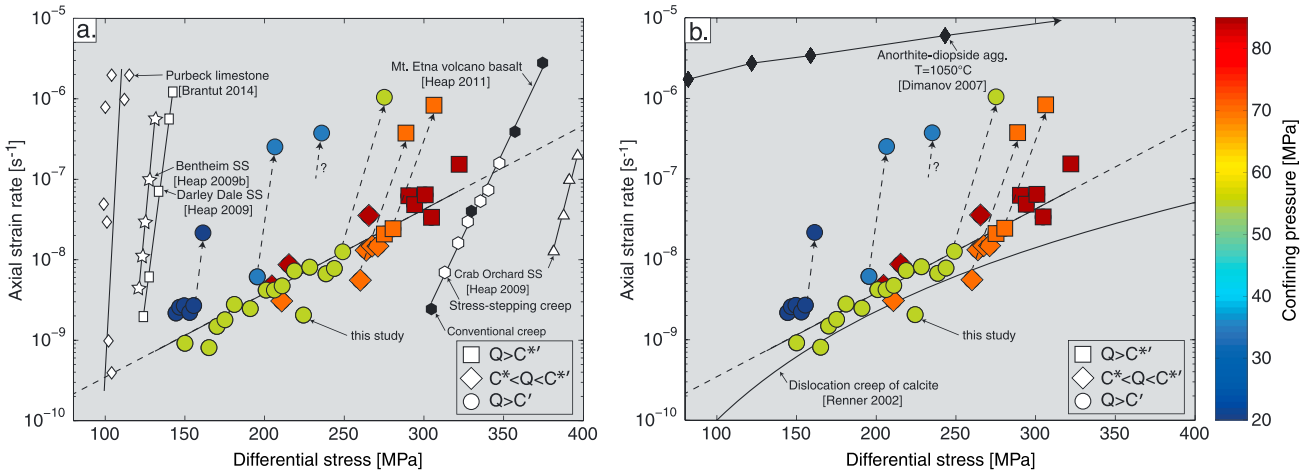

Figure 16. (a) Strain rate during secondary creep versus applied differential stress. Symbols and colors have the same meaning as in Figure 12. Strain rates during secondary creep obtained by *Heap et al.* [2009b] on Darley Dale, Bentheim, and Crab Orchard sandstones, by *Heap et al.* [2011] on Mount Etna volcano basalt and by *Brantut et al.* [2014] on Purbeck limestone below the brittle-ductile transition, are also shown for reference. (b) Same as Figure 16a. Strain rates during secondary creep obtained by *Dimanov et al.* [2007] on anorthite-diopside aggregates at $T = 1050°C$ are also shown for reference. Fitting their data on dislocation creep in calcite at temperatures in the range 873–1073 K, *Renner et al.* [2002] found a stress sensitivity of strain rate $n = 4.5$. This evolution of strain rate during secondary creep for such a stress sensitivity is shown for reference.

[*Johnson and Paris*, 1968; *Scholz*, 1968; *Kranz*, 1979; *Atkinson*, 1984; *Heap et al.*, 2009a; *Mallet et al.*, 2015a] reviewed in *Brantut et al.* [2013]. Thus, limestones deformed under constant stress conditions can undergo brittle creep, as recently shown by *Brantut et al.* [2014]. To overcome problems of sample variability among others, *Brantut et al.* [2014] offset the stress scale by the differential stress reached when deformation becomes dominated by dilatancy, denoted D' and corresponding to the minimum in porosity. They found that the minimum strain rate could be described by

$$\min\{\dot{\varepsilon}\} \propto \exp\left(\frac{Q - Q_{D'}}{\sigma^*}\right), \tag{3}$$

where $Q_{D'}$ is the differential stress reached when deformation becomes dominated by dilatancy and σ^* is an activation stress. At a given confining pressure, $Q_{D'}$ is a constant and this expression gives an activation stress similar to the one in equation (2).

Ashby and Sammis [1990], *Deshpande and Evans* [2008], *Bhat et al.* [2012], *Brantut et al.* [2012], and *Mallet et al.* [2015a] among others showed that brittle creep can be modeled adequately by the propagation of wing cracks from initial monosized flaws, a geometry in good agreement with direct observations on limestone by *Olsson* [1974]. Since subcritical crack growth is thermally activated, the growth of crack length (l) can be described using the law proposed by *Darot and Guéguen* [1986] and *Mallet et al.* [2015a]:

$$\frac{dl}{dt} = \dot{l}_0 \exp\left(\frac{-E_a}{kT}\right) \exp\left[\frac{s}{kT}\left(\frac{K_I^2}{E_0} - 2\gamma\right)\right], \tag{4}$$

where $\dot{l}_0$ is a characteristic crack speed dependent on the interatomic distance and atomic vibration frequency, E_a is an activation energy, s is an elementary surface, k is Boltzmann's constant, T is temperature, K_I is the stress intensity factor, and γ is the surface energy. *Mallet et al.* [2015a] showed that this crack growth law leads to an exponential relation between differential stress and strain rates, as described by equation (3).

During constant stress steps conducted at $P_c \leq 35$ MPa, axial deformation is associated with dilatancy and decreases in ultrasonic wave velocities from which we inferred an increase in crack density (Figures 6b, 7, and 11a) due to crack propagation, consistent with postdeformation microstructural observations of samples deformed at $P_c \leq 35$ MPa, which show few twinned grains but abundant cracks (Figures 13c–13f). Therefore, twinning does not appear to be the main deformation mechanism at these confining pressures. Furthermore, shear bands inclined to the vertical axis are observed in samples recovered from the vessel after deformation (Figures 13a and 13b).

Strain rates are strongly dependent on the applied differential stress for a range of brittle materials (Figure 16a). Focusing on the minimum strain rate, *Brantut et al.* [2014] found an activation stress $\sigma^* = 1.9$ MPa

for Purbeck limestone, close to $\sigma^* = 3$ MPa found for our experiments performed at $P_c = 20$ MPa and 35 MPa (Figure 16).

4.1.2. Semibrittle Creep

At constant stress and $P_c \geq 55$ MPa, the axial deformation is coupled either to inelastic compaction (at moderate differential stress) or to dilatancy (at the highest differential stresses). Micromechanisms of deformation during compactive and dilatant creep steps are examined separately hereafter.

4.1.2.1. Semibrittle Compactive Creep

Samples deformed at moderate constant differential stresses in the semibrittle regime ($P_c \geq 55$ MPa) undergo inelastic compaction. Several types of phenomena can account for inelastic compaction: (i) Hertzian fracture processes inducing grain crushing [e.g., *Zhang et al.*, 1990], sometimes with localization in compaction bands [e.g., *Fortin et al.*, 2005], (ii) grain rotations and rearrangements [e.g., *Tsai et al.*, 2003; *Karner et al.*, 2003; *Regnet et al.*, 2015b], (iii) intergranular pressure solution [e.g., *Zhang and Spiers*, 2005; *Zhang et al.*, 2010; *Gratier et al.*, 2013], or (iv) crystal plasticity (twinning, dislocation glides) [e.g., *Fredrich et al.*, 1989; *Dresen and Evans*, 1993]. All these phenomena can lead to time-dependent compactive deformation under constant stress [e.g., *Dusseault and Fordham*, 1993; *Heap et al.*, 2015].

Microstructural observations do not show any evidence of grain crushing, grain rotations, and rearrangements in samples of Tavel limestone deformed in stress-stepping semibrittle creep experiments (Figure 14). Moreover, ultrasonic wave velocities remain constant during secondary creep of each compactive steps (e.g., Figures 8d and 9d), contrary to what is observed during compaction due to grain crushing [*Fortin et al.*, 2005, 2007]. The evolution of the minimum strain rate with changing differential stress follows equation (2) with an activation stress of $\sigma^* = 38$ MPa (Figure 12a), far higher than that observed during brittle creep [*Heap et al.*, 2009b, 2011; *Brantut et al.*, 2014] and during the compactive creep experiments associated with the formation of compaction bands performed by *Heap et al.* [2015], who found an activation stress $\sigma^* = 4.1$ MPa. Since the sensitivity of the crack growth rate on the energy release rate at the crack tip in calcite is close to that of quartz [*Røyne et al.*, 2011; *Darot and Guéguen*, 1986], this difference implies that grain crushing (Hertzian fracture process) is not the main mechanism that controls the strain rate in Tavel limestone during creep in the semibrittle regime. This conclusion is in agreement with results from constant strain rate deformation experiments performed on Tavel limestone [*Vajdova et al.*, 2010; *Zhu et al.*, 2010; *Nicolas et al.*, 2016].

Our samples likely contain some water along the grain boundaries, potentially enabling pressure solution processes at rates comparable to the observed creep rates [e.g., *Zhang and Spiers*, 2005; *Zhang et al.*, 2010; *Gratier et al.*, 2013; *Brantut et al.*, 2014] because the solubility of calcite is high, even at room temperature. Direct observations of microstructural evidences for pressure solution were, however, not found but the small grain size of the micritic matrix makes observations difficult. As a conclusion, pressure solution cannot be ruled out as a possible mechanism but quantification of its contribution is difficult.

Processes such as mechanical twinning and dislocation slip are observed in the semibrittle deformation of carbonate rocks during constant strain rate deformation [e.g., *Olsson and Peng*, 1976; *Fredrich et al.*, 1989; *Baud et al.*, 2000a; *Nicolas et al.*, 2016]. *Baud et al.* [2000a] found that their data on the onset of inelastic compaction were in reasonable agreement with the plastic pore collapse model by *Curran and Carroll* [1979]. The most commonly used relation for dislocation creep is the power law creep equation:

$$\dot{\varepsilon} = \dot{\varepsilon}_0 \sigma^n \exp\left(-\frac{E_c}{\mathrm{RT}}\right), \tag{5}$$

where $\dot{\varepsilon}_0$ is a pre-exponential factor, σ is the differential stress, n is an index of the stress sensitivity of strain rate, E_c is the activation energy for creep, and RT is the standard Boltzmann term [*Kohlstedt et al.*, 1995]. Relation (5) is conventionally considered to apply to temperatures at (and above) about half the melting temperature [*Kohlstedt et al.*, 1995]; relations for lower temperatures have been presented too [e.g., *Weertman and Hecker*, 1983]. Fitting their data on dislocation creep in calcite at temperatures in the range 873–1073 K, *Renner et al.* [2002] found a stress exponent of $n = 4.5$. *Schmid* [1976] showed a transition from power law creep with n values around 4.5 to lower n values around 2 toward low stresses and suggested that the mechanisms associated with low n values are probably the active ones in many geological situations involving flow in fine-grained carbonate rocks and that they correspond to superplastic phenomena. The strain rate variation with differential stress is close to a power law with an exponent of 4.5 for our semibrittle creep experiments (Figure 16). Furthermore, *Dimanov et al.* [2007] deformed an anorthite-diopside aggregate at $T = 1050°C$ at constant stress. They interpreted their deformation as due to dislocations and found a stress sensitivity of

strain rate n in the range 0.6–1.2. Part of their data is shown in Figure 16. Although (i) temperatures are much higher and (ii) the material used is not calcite, strain rate during plastic deformation has a dependence on differential stress which is similar to what is observed during our semibrittle creep experiments. Finally, microstructural observations show a high twinning (Figures 14a and 14b) and dislocation density, especially along grain boundaries (Figure 15c). These observations suggest that plasticity (dislocation glide and twinning) controls the strain rate in Tavel limestone during compactive semibrittle creep, even though pressure solution may play a role.

4.1.2.2. Semibrittle Dilatant Creep

The found switch from compaction to dilation with increasing stress is similar to observations for low-porosity limestones deformed at constant strain rate in the semibrittle regime [e.g., *Baud et al.*, 2000a]. At room temperature, in calcite, dislocations and twins are blocked at grain boundaries, which creates an internal stress sufficient to nucleate cracks [e.g., *Smith and Barnby*, 1967; *Olsson and Peng*, 1976; *Evans et al.*, 1980; *Wong*, 1990], leading to dilatancy [e.g., *Baud et al.*, 2000a; *Nicolas et al.*, 2016]. *Stroh*, 's [1957] model for microcrack nucleation due to dislocation pileup is commonly used to analyze the transition from shear-enhanced compaction to dilatant cataclastic flow [*Baud et al.*, 2000a], but twins could also be considered in a similar manner [*Olsson and Peng*, 1976]. We suggest that dilatancy in the semibrittle regime is due to crack nucleation and/or propagation generated by twin and/or dislocation pileups, in agreement with microstructural observations (Figures 14 and 15c). Yet the evolution of minimum strain rate with differential stress follows the same trend during compactant and dilatant steps (Figure 12), suggesting the same controlling mechanism during all steps, except the last step which leads to failure in tertiary creep. We deduce that crack nucleation and/or propagation are controlled by the number of dislocations moving in pileups (i.e., plasticity), which explains why minimum strain rates follow the same trend during compacting and dilatant stress step (Figure 12). However, ultrasonic wave velocities remain constant—meaning the crack density is constant—during some dilatant secondary creep deformation whereas they decrease during primary creep at the same stress step (e.g., stress step presented in Figure 9), which implies limited crack propagation during secondary creep or a competition between pore closure and creation of new voids that shifts with increasing stress.

A break in slope can be observed in the σ-$\dot{\epsilon}_{ax}$ plot between the two last stress steps leading to failure in tertiary creep (Figure 12 b). Between these two steps, the activation stress is 6 MPa (Figure 12 b). This activation stress is much lower than that observed during the previous steps (38 MPa), and very close to that observed in brittle creep ($\sigma^* = 3$ MPa). Moreover, the decrease of ultrasonic wave velocities during the last stress steps at high confining pressure is consistent with crack propagation and eventual crack nucleation. We suggest that at this deformation stage, crack interaction becomes dominant and controls crack propagation, as observed during tertiary creep in the brittle field [e.g., *Brantut et al.*, 2012]. The difference of activation stress compared to that inferred from experiments performed in the brittle regime (6 MPa versus 3 MPa) could be due to the simultaneous occurrence of several mechanisms, i.e., cracking and plasticity.

4.2. Transient Inelastic Compaction: Its Stabilizing Role and Upper Limit

The final strain at failure increases with confining pressure from 0.8 to 2.6% and 3.9 to 10.2% below and above the brittle-ductile transition, respectively (inset in Figure 5a). This difference between samples below and above the brittle-ductile transition suggests that strains at failure are significantly affected by the dilatancy because of the work done by the confining pressure [*Edmond and Paterson*, 1972]. Macroscopic failure is due to the development of a macrofault. If damage is highly localized, failure will occur at a low final strain whereas the medium will be able to sustain a high damage before macroscopic failure if damage is homogeneously distributed.

For constant strain rate and stress-stepping experiments, the maximum compaction at the onset of postyield dilatancy $C^{*\prime}$ is slightly lower than 1%, far below the initial porosity value of 14.7%. Thus, we conclude that porosity is not the limiting parameter of the compaction process and we focus on plastic phenomena to explain the maximum inelastic compaction. The strain rate induced by dislocation slip is [*Orowan*, 1954]

$$\dot{\epsilon} = \rho_d \, b \, \langle v \rangle, \tag{6}$$

where ρ_d is the dislocation density, b is their Burgers vector and $\langle v \rangle$ is their average slip speed. Integrating equation (6) over a characteristic grain size d_g and assuming that dislocations cannot be eliminated at room temperature, one gets $\rho_d = \epsilon / b d_g$. Taking $b = 5 \times 10^{-10}$ m [*De Bresser*, 1996], $d_g \sim 5 \times 10^{-6}$ m, and $\epsilon \sim 1\%$, we estimate a dislocation density of $\rho_d = 4 \times 10^{12}$ m^{-2} comparable to observations on significantly deformed materials [*Fredrich et al.*, 1989; *Dimanov et al.*, 2007]. In calcite deformed at low temperature, dislocations and

twins accumulate at grain boundaries and other obstacles, and this high dislocation density could induce stresses sufficient to initiate cracking [e.g., *Stroh*, 1954; *Smith and Barnby*, 1967; *Olsson and Peng*, 1976; *Wong*, 1990]. Thus, the maximum compaction at a given confining pressure could be limited by the dislocation density (thus by the grain size and the inelastic strain) rather than controlled by differential stress.

Elastic wave velocities remain constant during compaction in the semibrittle regime (Figure 8), indicating little (or no) crack propagation. Thus, compactive semibrittle steps might not lead to macroscopic failure under constant stress, even if failure cannot be totally excluded since intragranular plasticity can lead to crack nucleation [e.g., *Stroh*, 1954; *Smith and Barnby*, 1967; *Olsson and Peng*, 1976; *Wong*, 1990]. Given the very low strain rates in the semibrittle compactive steps ($\sim 10^{-9}$ s^{-1}, see section 3.3) and the strains sustained by samples deformed in the semibrittle regime, failure could possibly happen after $\sim 10^{8}$ s, i.e., approximately 1150 days, and this could not be verified experimentally. The possibility for a sample to go through the $C^{*\prime}$ transition and ultimately failure under constant load remains open and probably depends on how far the applied stress state is from $C^{*\prime}$ inferred from constant strain rate experiments.

4.3. Implications

Compaction is sometimes induced by the production of reservoirs [*Fredrich et al.*, 2000] and can cause subsidence [e.g., *Morton et al.*, 2006], which requires to redesign offshore platforms, or can induce seismicity [e.g., *Segall*, 1989] and well failure [e.g., *Bruno*, 1992], among other problems [*Nagel*, 2001]. A recent study by *Heap et al.* [2015] showed that time-dependent compaction in sandstones can be caused by the development of compaction bands, which can cause barriers for fluid flow because of the heterogeneous deformation. Our study highlights that time-dependent compaction can be induced by plasticity in carbonate rocks deformed at room temperature and moderate pressure. The deformation is much more homogeneous than in the case of compaction band development but could still induce a change in permeability [*Xiao et al.*, 2006]. It is difficult to predict the bulk effect of the competing processes, permeability reduction due to plasticity accommodated compaction and permeability increase due to dilatant microcracking. Thus, the semibrittle behavior of limestone at constant stress should be pursued, especially focusing on the roles of temperature and pore fluids on the mechanical behavior and focusing on the evolution of permeability during inelastic compaction and dilatancy.

At the scale of the lithosphere, quantitative predictions of the strength are based on experimentally determined constitutive equations acquired through constant strain rate experiments [e.g., *Brace and Kohlstedt*, 1980; *Kirby*, 1980] performed at rates that significantly exceed natural rates. In the upper portion of the lithosphere, a relation for frictional sliding is used to describe the deformation on a brittle fault [e.g., *Sibson*, 1974; *Byerlee*, 1978; *Chester*, 1995]. For the deeper part of the lithosphere, power law creep equations are used to estimate the plastic flow strength [e.g., *Weertman et al.*, 1978; *Guéguen and Palciauskas*, 1994]. Our experiments emphasize the importance of the semibrittle behavior, as observed in some natural settings [e.g., *Ross and Lewis*, 1989]. In this regime, a mixed behavior between plastic phenomena and brittle behavior is observed, which makes it difficult to derive a single constitutive equation based on micromechanical observations for deformation behavior [e.g., *Ross and Lewis*, 1989] although our results suggest the same strain rate sensitivity to differential stress for semibrittle deformation with dominant compaction and semibrittle deformation with dominant dilatancy. Note, however, that our experiments were performed under ambient humidity conditions and that in natural settings the presence of fluids could lead to micromechanisms of deformation that were not considered in this paper.

5. Conclusion

We investigated the creep behavior of a limestone with an initial porosity of 14.7%. Brittle or semibrittle deformation occurs depending on the confining pressure. Based on the observation of dilatancy coupled to a decrease of elastic wave velocities during all stress steps and in agreement with microstructural observations and previous studies, we conclude that subcritical crack growth is responsible for the deformation observed under constant stress at $P_c \leq 35$ MPa (brittle regime). Brittle creep of the limestone is associated with dilatancy and the development of a shear fault at final strains lower than 2%, as previously observed for other brittle materials. Semibrittle creep leads to inelastic compaction accommodated by crystal plasticity and then to dilatancy likely due to the nucleation and propagation of cracks at dislocation pileups. Pressure solution also potentially took place since samples were open to ambient air during deformation.

The strain rate during secondary creep is sensitive to stress in the brittle regime. In the semibrittle regime, two trends can be observed in the σ-$\dot{\epsilon}_{ax}$ plot. When crystal plasticity is dominant, the strain rate during secondary creep is not significantly stress dependent, as observed in fully plastic materials at high temperatures. As failure by tertiary creep is approached, the strain rate during secondary creep becomes stress dependent, as for brittle creep.

Acknowledgments
The data used are listed in Table 1 and shown in figures. The first author thanks Patrick Baud and Serge Lugan for providing the block of Tavel limestone. The authors are grateful to Simon Hallais, Alexandre Tanguy, Damien Deldicque, Yves Pinquier, and Serguei Matveev for technical support. A.N. is also grateful to Philippe Marchina, Teng-Fong Wong, Yves M. Leroy, Alexandre Schubnel, Harsha S. Bhat, Patrick Baud, Christian David, Francois Passelegue, and Philippe Robion for stimulating discussions. The authors are indebted to Patrick Baud, Joerg Renner, an anonymous reviewer, and an Associate Editor for their constructive comments, which led to significant improvements of the manuscript. This project was funded by a grant provided by TotalFR00006158.

References

Amitrano, D., and A. Helmstetter (2006), Brittle creep, damage, and time to failure in rocks, *J. Geophys. Res.*, *111*, B11201, doi:10.1029/2005JB004252.
Ashby, M., and C. G. Sammis (1990), The damage mechanics of brittle solids in compression, *Pure Appl. Geophys.*, *133*, 489–521.
Atkinson, B. K. (1984), Subcritical crack growth in geological materials, *J. Geophys. Res.*, *89*(B6), 4077–4114.
Atkinson, B. K., and P. Meredith (1987), Fracture mechanics of rock, in *The Theory of Subcritical Crack Growth With Applications to Minerals and Rocks*, pp. 111–166, Academic Press, London.
Ayling, M. R., P. G. Meredith, and S. A. Murrell (1995), Microcracking during triaxial deformation of porous rocks monitored by changes in rock physical properties, I. Elastic-wave propagation measurements on dry rocks, *Tectonophysics*, *245*(3), 205–221.
Baud, P., A. Schubnel, and T.-F. Wong (2000a), Dilatancy, compaction, and failure mode in Solnhofen limestone, *J. Geophys. Res.*, *105*(B8), 19,289–19,303, doi:10.1029/2000JB900133.
Baud, P., W. Zhu, and T.-f. Wong (2000b), Failure mode and weakening effect of water on sandstone, *J. Geophys. Res.*, *105*(B7), 16,371–16,389, doi:10.1029/2000JB900087.
Benson, P., A. Schubnel, S. Vinciguerra, C. Trovato, P. Meredith, and R. P. Young (2006), Modeling the permeability evolution of microcracked rocks from elastic wave velocity inversion at elevated isostatic pressure, *J. Geophys. Res.*, *111*, B04202, doi:10.1029/2005JB003710.
Bhat, H. S., A. J. Rosakis, and C. G. Sammis (2012), A micromechanics based constitutive model for brittle failure at high strain rates, *J. Appl. Mech.*, *79*(3), 31016, doi:10.1115/1.4005897.
Brace, W. (1978), Volume changes during fracture and frictional sliding: A review, *Pure Appl. Geophys.*, *116*, 603–614.
Brace, W., and D. Kohlstedt (1980), Limits on lithospheric stress imposed by laboratory experiments, *J. Geophys. Res.*, *85*(B11), 6248–6252.
Brantut, N. (2015), Time-dependent recovery of microcrack damage and seismic wave speeds in deformed limestone, *J. Geophys. Res. Solid Earth*, *120*, 8088–8109, doi:10.1002/2015JB012324.
Brantut, N., A. Schubnel, and Y. Guéguen (2011), Damage and rupture dynamics at the brittle-ductile transition: The case of gypsum, *J. Geophys. Res.*, *116*, B01404, doi:10.1029/2010JB007675.
Brantut, N., P. Baud, M. Heap, and P. Meredith (2012), Micromechanics of brittle creep in rocks, *J. Geophys. Res.*, *117*, B08412, doi:10.1029/2012JB009299.
Brantut, N., M. Heap, P. Meredith, and P. Baud (2013), Time-dependent cracking and brittle creep in crustal rocks: A review, *J. Struct. Geol.*, *52*, 17–43.
Brantut, N., M. J. Heap, P. Baud, and P. G. Meredith (2014), Mechanisms of time-dependent deformation in porous limestone, *J. Geophys. Res. Solid Earth*, *119*, 5444–5463, doi:10.1002/2014JB011186.
Bruno, M. (1992), Subsidence-induced well failure, *SPE Drill. Eng.*, *7*(02), 148–152.
Budiansky, B., and R. J. O'Connell (1976), Elastic moduli of a cracked solid, *Int. J. Solids Struct.*, *12*(2), 81–97, doi:10.1016/0020-7683(76)90044-5.
Byerlee, J. D. (1968), Brittle-ductile transition in rocks, *J. Geophys. Res.*, *73*(14), 4741–4750.
Byerlee, J. D. (1978), Friction of rocks, *Pure Appl. Geophys.*, *116*(4–5), 615–626.
Charles, R. (1958), Static fatigue of glass. I., *J. Appl. Phys.*, *29*(11), 1549–1553.
Cheng, Y., L. N. Y. Wong, and V. Maruvanchery (2016), Transgranular crack nucleation in Carrara marble of brittle failure, *Rock Mech. Rock Eng.*, *49-8*, 3069–3082.
Chester, F. M. (1995), A rheologic model for wet crust applied to strike-slip faults, *J. Geophys. Res.*, *100*(B7), 13,033–13,044.
Clarke, D., B. Lawn, and D. Roach (1986), *The Role of Surface Forces in Fracture*, pp. 341–350, Springer, New York.
Costin, L. (1987), Fracture mechanics of rock, in *Time-Dependent Deformation and Failure*, pp. 167–216, Academic Press, London.
Covey-Crump, S., W. Xiao, J. Mecklenburgh, E. Rutter, and S. May (2016), Exploring the influence of loading geometry on the plastic flow properties of geological materials: Results from combined torsion + axial compression tests on calcite rocks, *J. Struct. Geol.*, *88*, 20–31.
Curran, J. H., and M. M. Carroll (1979), Shear stress enhancement of void compaction, *J. Geophys. Res.*, *84*(B3), 1105–1112, doi:10.1029/JB084iB03p01105.
Darot, M., and Y. Guéguen (1986), Slow crack growth in minerals and rocks: Theory and experiments, *Pure Appl. Geophys.*, *124*(4–5), 677–692.
Dautriat, J., M. Bornert, N. Gland, A. Dimanov, and J. Raphanel (2011), Localized deformation induced by heterogeneities in porous carbonate analysed by multi-scale digital image correlation, *Tectonophysics*, *503*(1), 100–116.
De Bresser, J. (1996), Steady state dislocation densities in experimentally deformed calcite materials: Single crystals versus polycrystals, *J. Geophys. Res.*, *101*(B10), 22,189–22,201.
De Bresser, J., and C. Spiers (1993), Slip systems in calcite single crystals deformed at 300–800 C, *J. Geophys. Res.*, *98*(B4), 6397–6409.
De Bresser, J., and C. Spiers (1997), Strength characteristics of the *r*, *f*, and *c* slip systems in calcite, *Tectonophysics*, *272*(1), 1–23.
De Bresser, J., J. Urai, and D. Olgaard (2005), Effect of water on the strength and microstructure of Carrara marble axially compressed at high temperature, *J. Struct. Geol.*, *27*(2), 265–281.
Deshpande, V., and A. G. Evans (2008), Inelastic deformation and energy dissipation in ceramics: A mechanism-based constitutive model, *J. Mech. Phys. Solids*, *56*, 3077–3100.
Dimanov, A., E. Rybacki, R. Wirth, and G. Dresen (2007), Creep and strain-dependent microstructures of synthetic anorthite–diopside aggregates, *J. Struct. Geol.*, *29*(6), 1049–1069.
Dresen, G., and B. Evans (1993), Brittle and semibrittle deformation of synthetic marbles composed of two phases, *J. Geophys. Res.*, *98*(B7), 11,921–11,933.
Dunning, J., B. Douglas, M. Miller, and S. McDonald (1994), The role of the chemical environment in frictional deformation: Stress corrosion cracking and comminution, *Pure Appl. Geophys.*, *143*(1–3), 151–178.
Dusseault, M. B., and C. J. Fordham (1993), Time-dependent behavior of rocks, in *Comprehensive Rock Engineering Principles, Practice and Project: Rock Testing and Site Characterization*, vol. 3, pp. 119–149, Pergamon Press, Oxford, U. K.

Edmond, J., and M. Paterson (1972), Volume changes during the deformation of rocks at high pressures, *Int. J. Rock Mech. Mining Sci.*, *9*(2), 161–182.
Eslami, J., D. Hoxha, and D. Grgic (2012), Estimation of the damage of a porous limestone using continuous wave velocity measurements during uniaxial creep tests, *Mech. Mater.*, *49*, 51–65.
Evans, A., M. Meyer, K. Fertig, B. Davis, and H. Baumgartner (1980), Probabilistic models for defect initiated fracture in ceramics, *J. Nondestruct. Evaluat.*, *1*(2), 111–122.
Evans, B., J. T. Fredrich, and T.-f. Wong (1990), The brittle-ductile transition in rocks: Recent experimental and theoretical progress, in *The Brittle-Ductile Transition in Rocks, The Heard Volume, Am. Geophys. Monogr.*, vol. 56, edited by A. Duba et al., pp. 1–20, AGU, Washington, D. C.
Faleskog, J., and C. F. Shih (1997), Micromechanics of coalescence? I. Synergistic effects of elasticity, plastic yielding and multi-size-scale voids, *J. Mech. Phys. Solids*, *45*(1), 21–50.
Fortin, J., A. Schubnel, and Y. Guéguen (2005), Elastic wave velocities and permeability evolution during compaction of bleurswiller sandstone, *Int. J. Rock Mech. Mining Sci.*, *42*(7), 873–889.
Fortin, J., Y. Guéguen, and A. Schubnel (2007), Effects of pore collapse and grain crushing on ultrasonic velocities and V_p/V_s, *J. Geophys. Res.*, *112*, B08207, doi:10.1029/2005JB004005.
Fortin, J., S. Stanchits, S. Vinciguerra, and Y. Guéguen (2011), Influence of thermal and mechanical cracks on permeability and elastic wave velocities in a basalt from Mt. Etna volcano subjected to elevated pressure, *Tectonophysics*, *503*(1), 60–74.
Fredrich, J. T., B. Evans, and T.-f. Wong (1989), Micromechanics of the brittle to plastic transition in Carrara marble, *J. Geophys. Res.*, *94*(B4), 4129–4145, doi:10.1029/JB094iB04p04129.
Fredrich, J. T., B. Evans, and T.-F. Wong (1990), Effect of grain size on brittle and semibrittle strength: Implications for micromechanical modelling of failure in compression, *J. Geophys. Res.*, *95*(B7), 10,907–10,920.
Fredrich, J. T., J. G. Arguello, G. L. Deitrick, and E. P. de Rouffignac (2000), Geomechanical modeling of reservoir compaction, surface subsidence, and casing damage at the Belridge diatomite field, in *SPE Reservoir Evaluation and Engineering*, vol. 3, pp. 348–359, Soc. Pet. Eng.
Ghabezloo, S. (2015), A micromechanical model for the effective compressibility of sandstones, *Eur. J. Mech.*, *51*, 140–153.
Gratier, J.-P., D. K. Dysthe, and F. Renard (2013), The role of pressure solution creep in the ductility of the Earth's upper crust, *Adv. Geophys.*, *54*, 47–179.
Grechka, V., and M. Kachanov (2006), Effective elasticity of fractured rocks: A snapshot of the work in progress, *Geophysics*, *71*, W45–W58.
Griggs, D. T., F. J. Turner, and H. C. Heard (1960), Chapter 4: Deformation of rocks at 500° to 800°C, *Geol. Soc. Am. Mem.*, *79*, 39–104, doi:10.1130/MEM79-p39.
Guéguen, Y., and M. Kachanov (2011), Effective elastic properties of cracked rocks—An overview, in *Mechanics of Crustal Rocks*, pp. 73–125, Springer, Vienna.
Guéguen, Y., and V. Palciauskas (1994), *Introduction to the Physics of Rocks*, Princeton Univ. Press, Princeton, N. J.
Heap, M., P. Baud, P. Meredith, A. Bell, and I. Main (2009a), Time-dependent brittle creep in Darley Dale sandstone, *J. Geophys. Res.*, *114*, B07203, doi:10.1029/2008JB006212.
Heap, M., P. Baud, and P. Meredith (2009b), Influence of temperature on brittle creep in sandstones, *Geophys. Res. Lett.*, *36*, L19305, doi:10.1029/2009GL039373.
Heap, M., P. Baud, P. Meredith, S. Vinciguerra, A. Bell, and I. Main (2011), Brittle creep in basalt and its application to time-dependent volcano deformation, *Earth Planet. Sci. Lett.*, *307*(1), 71–82.
Heap, M. J., N. Brantut, P. Baud, and P. G. Meredith (2015), Time-dependent compaction band formation in sandstone, *J. Geophys. Res. Solid Earth*, *120*, 4808–4830, doi:10.1002/2015JB012022.
Heard, H. C. (1960), Chapter 7: Transition from brittle fracture to ductile flow in Solenhofen limestone as a function of temperature, confining pressure, and interstitial fluid pressure, *Geol. Soc. Am. Mem.*, *79*, 193–226, doi:10.1130/MEM79-p193.
Henry, J. P., J. Paquet, and J. Tancrez (1977), Experimental study of crack propagation in calcite rocks, *Int. J. Rock Mech. Mining Sci. Geomech. Abstr.*, *14*(2), 85–91.
Hirth, J., and R. Balluffi (1973), On grain boundary dislocations and ledges, *Acta Metall.*, *21*(7), 929–942.
Holder, J., J. E. Olson, and Z. Philip (2001), Experimental determination of subcritical crack growth parameters in sedimentary rock, *Geophys. Res. Lett.*, *28*(4), 599–602.
Johnson, H. H., and P. C. Paris (1968), Sub-critical flaw growth, *Eng. Fracture Mech.*, *1*(1), 3–45.
Karner, S. L., F. M. Chester, A. K. Kronenberg, and J. S. Chester (2003), Subcritical compaction and yielding of granular quartz sand, *Tectonophysics*, *377*(3), 357–381.
Kinloch, A., and J. Williams (1980), Crack blunting mechanisms in polymers, *J. Mater. Sci.*, *15*(4), 987–996.
Kirby, S. H. (1980), Tectonic stresses in the lithosphere: Constraints provided by the experimental deformation of rocks, *J. Geophys. Res.*, *85*(B11), 6353–6363.
Kohlstedt, D., et al. (1995), Strength of the lithosphere: constraints imposed by laboratory experiments, *J. Geophys. Res.*, *100*, 17–587.
Kranz, R. L. (1979), Crack growth and development during creep of Barre granite, *Int. J. Rock Mech. Mining Sci. Geomech. Abstr.*, *16*(1), 23–35.
Liteanu, E., C. Spiers, and J. de Bresser (2013), The influence of water and supercritical CO_2 on the failure behavior of chalk, *Tectonophysics*, *599*, 157–169.
Liu, Z., and J. Shao (2016), Strength behavior, creep failure and permeability change of a tight marble under triaxial compression, *Rock Mech. Rock Eng.*, *50*, 529–541.
Lockner, D. (1993), Room temperature creep in saturated granite, *J. Geophys. Res.*, *98*(B1), 475–487.
Mallet, C., J. Fortin, Y. Guéguen, and F. Bouyer (2013), Effective elastic properties of cracked solids: An experimental investigation, *Int. J. Fracture*, *182*(2), 275–282.
Mallet, C., J. Fortin, Y. Guéguen, and F. Bouyer (2014), Evolution of the crack network in glass samples submitted to brittle creep conditions, *Int. J. Fracture*, *190*(1–2), 111–124.
Mallet, C., J. Fortin, Y. Guéguen, and F. Bouyer (2015a), Brittle creep and subcritical crack propagation in glass submitted to triaxial conditions, *J. Geophys. Res. Solid Earth*, *120*, 879–893, doi:10.1002/2014JB011231.
Mallet, C., J. Fortin, Y. Guéguen, and F. Bouyer (2015b), Role of the pore fluid in crack propagation in glass, *Mech. Time-Dependent Mater.*, *19*(2), 117–133.
Mavko, G., T. Mukerji, and N. Godfrey (1995), Predicting stress-induced velocity anisotropy in rocks, *Geophysics*, *60*(4), 1081–1087.
McMeeking, R. M. (1977), Finite deformation analysis of crack-tip opening in elastic-plastic materials and implications for fracture, *J. Mech. Phys. Solids*, *25*(5), 357–381.

Meredith, P., and B. Atkinson (1985), Fracture toughness and subcritical crack growth during high-temperature tensile deformation of Westerly granite and Black gabbro, *Phys. Earth Planet. Inter.*, *39*(1), 33–51.
Morton, R. A., J. C. Bernier, and J. A. Barras (2006), Evidence of regional subsidence and associated interior wetland loss induced by hydrocarbon production, Gulf Coast Region, USA, *Environ. Geol.*, *50*(2), 261–274.
Nagel, N. (2001), Compaction and subsidence issues within the petroleum industry: From Wilmington to Ekofisk and beyond, *Phys. Chem. Earth Part A*, *26*, 3–14.
Nasseri, M., A. Schubnel, and R. Young (2007), Coupled evolutions of fracture toughness and elastic wave velocities at high crack density in thermally treated Westerly granite, *Int. J. Rock Mech. Mining Sci.*, *44*(4), 601–616.
Nicolas, A., J. Fortin, J. Regnet, A. Dimanov, and Y. Guéguen (2016), Brittle and semi-brittle behaviours of a carbonate rock: Influence of water and temperature, *Geophys. J. Int.*, *206*(1), 438–456.
Olsson, W. A. (1974), Microfracturing and faulting in a limestone, *Tectonophysics*, *24*(3), 277–285.
Olsson, W. A., and S. S. Peng (1976), Microcrack nucleation in marble, *Int. J. Rock Mech. Mining Sci.*, *13*(2), 53–59.
Orowan, E. (1944), The fatigue of glass under stress, *Nature*, *154*(3906), 341–343.
Orowan, E. (1954), Dislocations in metals, 131 pp.
Ougier-Simonin, A., J. Fortin, Y. Guéguen, A. Schubnel, and F. Bouyer (2011), Cracks in glass under triaxial conditions, *Int. J. Eng. Sci.*, *49*(1), 105–121, doi:10.1016/j.ijengsci.2010.06.026.
Paterson, M. (1978), *Experimental Rock Deformation: The Brittle Field*, pp. 16–50, Springer, New York.
Paterson, M. S., and T.-f. Wong (2005), *Experimental Rock Deformation: The Brittle Field*, 2nd ed., Springer Verlag, Berlin.
Rebinder, P., L. Schreiner, and K. Zhigach (1948), Hardness reducers in rock drilling, 163 pp.
Regnet, J. B., P. Robion, C. David, J. Fortin, B. Brigaud, and B. Yven (2015a), Acoustic and reservoir properties of microporous carbonate rocks: Implication of micrite particle size and morphology, *J. Geophys. Res. Solid Earth*, *120*, 790–811, doi:10.1002/2014JB011313.
Regnet, J. B., C. David, J. Fortin, P. Robion, Y. Makhloufi, and P. Collin (2015b), Influence of microporosity distribution on the mechanical behaviour of oolithic carbonate rocks, *Geomech. Energy Environ.*, *3*, 11–23.
Renner, J., and F. Rummel (1996), The effect of experimental and microstructural parameters on the transition from brittle failure to cataclastic flow of carbonate rocks, *Tectonophysics*, *258*(1), 151–169.
Renner, J., B. Evans, and G. Siddiqi (2002), Dislocation creep of calcite, *J. Geophys. Res.*, *107*(B12), 2364, doi:10.1029/2001JB001680.
Ross, J. V., and P. D. Lewis (1989), Brittle-ductile transition: Semi-brittle behavior, *Tectonophysics*, *167*(1), 75–79.
Rostom, F., A. Røyne, D. K. Dysthe, and F. Renard (2013), Effect of fluid salinity on subcritical crack propagation in calcite, *Tectonophysics*, *583*, 68–75.
Røyne, A., D. Dysthe, and J. Bisschop (2008), Mechanisms of subcritical cracking in calcite, Abstract MR33B-1857 presented at 2008 Fall Meeting, AGU, San Francisco, Calif.
Røyne, A., J. Bisschop, and D. K. Dysthe (2011), Experimental investigation of surface energy and subcritical crack growth in calcite, *J. Geophys. Res.*, *116*, B04204, doi:10.1029/2010JB008033.
Rutter, E. (1972), The effects of strain-rate changes on the strength and ductility of Solenhofen limestone at low temperatures and confining pressures, *Int. J. Rock Mech. Min. Sci.*, *9*(2), 183–189.
Rutter, E. H. (1974), The influence of temperature, strain rate and interstitial water in the experimental deformation of calcite rocks, *Tectonophysics*, *22*(3), 311–334.
Sayers, C. M., and M. Kachanov (1995), Microcrack-induced elastic wave anisotropy of brittle rocks, *J. Geophys. Res.*, *100*(B3), 4149–4156, doi:10.1029/94JB03134.
Schmid, S. (1976), Rheological evidence for changes in the deformation mechanism of Solenhofen limestone towards low stresses, *Tectonophysics*, *31*(1), T21–T28.
Scholz, C. (1968), Mechanism of creep in brittle rock, *J. Geophys. Res.*, *73*(10), 3295–3302.
Schubnel, A., J. Fortin, L. Burlini, and Y. Guéguen (2005), Damage and recovery of calcite rocks deformed in the cataclastic regime, *Geol. Soc. London Spec. Publ.*, *245*(1), 203–221, doi:10.1144/GSL.SP.2005.245.01.10.
Schubnel, A., E. Walker, B. D. Thompson, J. Fortin, Y. Guéguen, and R. P. Young (2006), Transient creep, aseismic damage and slow failure in Carrara marble deformed across the brittle-ductile transition, *Geophys. Res. Lett.*, *33*, L17301, doi:10.1029/2006GL026619.
Segall, P. (1989), Earthquakes triggered by fluid extraction, *Geology*, *17*(10), 942–946.
Sibson, R. H. (1974), Frictional constraints on thrust, wrench and normal faults, *Nature*, *249*, 542–544, doi:10.1038/249542a0.
Smith, E., and J. Barnby (1967), Crack nucleation in crystalline solids, *Metal Sci.*, *1*(1), 56–64.
Stroh, A. (1954), The formation of cracks as a result of plastic flow, *Proc. R. Soc. London A*, *223*(1154), 404–414.
Stroh, A. N. (1957), A theory of the fracture of metals, *Adv. Phys.*, *6*(24), 418–465.
Swanson, P. L. (1984), Subcritical crack growth and other time-and environment-dependent behavior in crustal rocks, *J. Geophys. Res.*, *89*(B6), 4137–4152.
Tsai, J.-C., G. A. Voth, and J. P. Gollub (2003), Internal granular dynamics, shear-induced crystallization, and compaction steps, *Phys. Rev. Lett.*, *91*(6), 64301, doi:10.1103/PhysRevLett.91.064301.
Turner, F. J., D. T. Griggs, and H. Heard (1954), Experimental deformation of calcite crystals, *Geol. Soc. Am. Bull.*, *65*(9), 883–934, doi:10.1130/0016-7606(1954)65.
Vajdova, V., P. Baud, and T.-f. Wong (2004), Compaction, dilatancy, and failure in porous carbonate rocks, *J. Geophys. Res.*, *109*, B05204, doi:10.1029/2003JB002508.
Vajdova, V., W. Zhu, T.-M. N. Chen, and T.-f. Wong (2010), Micromechanics of brittle faulting and cataclastic flow in Tavel limestone, *J. Struct. Geol.*, *32*(8), 1158–1169, doi:10.1016/j.jsg.2010.07.007.
Vincké, O., M. Boutéca, J. Piau, and D. Fourmaintraux (1998), Poromechanics: A tribute to Maurice A. Biot, in *Study of the Effective Stress at Failure*, edited by J.-F. Thimus et al., pp. 635–639, A. A. Balkema, Rotterdam, Netherlands.
Wang, W., Y. Cao, Q. Zhu, W. Xu, and J. Shao (2015a), Experimental investigation and constitutive modelling of creep-damage behaviours in monzogranite, *Eur. J. Environ. Civil Eng.*, *19*(sup1), 54–69.
Wang, W., H.-X. Liu, Q.-Z. Zhu, and J.-F. Shao (2015b), A micromechanics-based creep damage model for brittle rocks, *Eur. J. Environ. Civil Eng.*, *19*(sup1), s1–s14.
Weertman, J., and S. Hecker (1983), Theory for saturation stress difference in torsion versus other types of deformation at low temperatures, *Mech. Mater.*, *2*(2), 89–101.
Weertman, J., S. White, and A. H. Cook (1978), Creep laws for the mantle of the Earth [and discussion], *Philos. Trans. R. Soc. London A*, *288*(1350), 9–26.
Wiederhorn, S., and L. Bolz (1970), Stress corrosion and static fatigue of glass, *J. Am. Ceramic Soc.*, *53*(10), 543–548.

Wirth, R. (2009), Focused Ion Beam (FIB) combined with SEM and TEM: Advanced analytical tools for studies of chemical composition, microstructure and crystal structure in geomaterials on a nanometre scale, *Chem. Geol.*, *261*(3), 217–229.

Wong, T.-f (1990), A note on the propagation behavior of a crack nucleated by a dislocation pileup, *J. Geophys. Res.*, *95*(B6), 8639–8646, doi:10.1029/JB095iB06p08639.

Wong, T.-f., and P. Baud (2012), The brittle-ductile transition in porous rock: A review, *J. Struct. Geol.*, *44*(0), 25–53, doi:10.1016/j.jsg.2012.07.010.

Wong, T.-f., C. David, and W. Zhu (1997), The transition from brittle faulting to cataclastic flow in porous sandstones: Mechanical deformation, *J. Geophys. Res.*, *102*(B2), 3009–3025, doi:10.1029/96JB03281.

Xiao, X., B. Evans, and Y. Bernabé (2006), Permeability evolution during non-linear viscous creep of calcite rocks, *Pure Appl. Geophys.*, *163*, 2071–2102, doi:10.1007/s00024-006-0115-1.

Zhang, J., T.-f. Wong, and D. M. Davis (1990), Micromechanics of pressure-induced grain crushing in porous rocks, *J. Geophys. Res.*, *95*(B1), 341–352.

Zhang, X., and C. Spiers (2005), Compaction of granular calcite by pressure solution at room temperature and effects of pore fluid chemistry, *Int. J. Rock Mech. Mining Sci.*, *42*(7), 950–960.

Zhang, X., C. J. Spiers, and C. J. Peach (2010), Compaction creep of wet granular calcite by pressure solution at 28° C to 150° C, *J. Geophys. Res.*, *115*, B09217, doi:10.1029/2008JB005853.

Zhu, W., P. Baud, and T.-F. Wong (2010), Micromechanics of cataclastic pore collapse in limestone, *J. Geophys. Res.*, *115*, B04405, doi:10.1029/2009JB006610.